JGR Oceans

RESEARCH ARTICLE
10.1029/2024JC022277

Hydrothermal Plume Near-Field Dynamics From LES and Observations

Cyprien Lemaréchal[1], **Guillaume Roullet**[1], **and Jonathan Gula**[1,2]

[1]University Brest, CNRS, Ifremer, IRD, Laboratoire d'Océanographie Physique et Spatiale (LOPS), IUEM, F29280, Plouzané, France, [2]Institut Universitaire de France (IUF), Paris, France

Key Points:

- High-resolution simulations characterize hydrodynamics of the near-field hydrothermal plume and show strong mixing with significant variability
- Hydrothermal plumes are found in a transitional regime in the first two meters, which is not taken into account by plume theory, and in a pure plume regime above this depth
- Short exposure times to high temperatures suggest that biological materials can be transported through the plume without lethal effects

Correspondence to:

G. Roullet,
roullet@univ-brest.fr

Citation:

Lemaréchal, C., Roullet, G., & Gula, J. (2025). Hydrothermal plume near-field dynamics from LES and observations. *Journal of Geophysical Research: Oceans*, *130*, e2024JC022277. https://doi.org/10.1029/2024JC022277

Received 19 DEC 2024
Accepted 29 SEP 2025

Author Contributions:

Conceptualization: Cyprien Lemaréchal, Guillaume Roullet
Formal analysis: Cyprien Lemaréchal, Guillaume Roullet
Funding acquisition: Guillaume Roullet, Jonathan Gula
Investigation: Cyprien Lemaréchal
Methodology: Cyprien Lemaréchal, Guillaume Roullet
Project administration: Guillaume Roullet, Jonathan Gula
Resources: Jonathan Gula
Supervision: Guillaume Roullet, Jonathan Gula
Validation: Guillaume Roullet
Visualization: Cyprien Lemaréchal
Writing – original draft: Cyprien Lemaréchal
Writing – review & editing: Guillaume Roullet, Jonathan Gula

Abstract Hydrothermal plumes play a crucial role in vent fields by injecting significant buoyancy flux from centimeter-scale vents and rising hundreds of meters. This is a multiscale process, yet only the large scales have been well studied. Near-vent dynamics remain a challenge in plume modeling, despite their importance for understanding deep-sea environments. Thus, this work addresses this gap by characterizing the near-field hydrodynamics and comparing it with plume theory and observations. We use a large-eddy simulation (LES) approach with adaptive mesh refinement, achieving centimeter-scale resolution within a 6-m domain above the vent. We first study a typical black smoker to quantify the mean flow and spatial variability, investigating the link between turbulent structures and the entrainment rate α of surrounding water. Significant vertical and temporal variability in α is observed, limiting the applicability of the theoretical model. The LES reproduces in situ data well. Next, we investigate the sensitivity of the flow to source parameters, from forced to lazy plumes. The results reveal a transition region between vent conditions to the pure plume regime, where flow self-similarity breaks down. This transition region is key to interpreting observations. Above this region, plumes achieve self-similarity, and the flow field becomes consistent with theoretical plume scaling, showing dependence on source buoyancy flux. Finally, we show that extreme temperatures above 100°C occur within the first two m of the plume, but exposure times for a proxy tracer are short. This suggests that hydrothermal plumes could serve as viable transport vectors for biological materials.

Plain Language Summary Hydrothermal vent fields on the ocean floor release hot, mineral-rich water that forms rising plumes, known as black smokers. These plumes are critical to the unique ecosystems around vents (the source points) and influence how heat and materials are spread through the ocean. However, the details of plume behavior near the seafloor, where they are most energetic, remain poorly understood. Using advanced computer simulations, we studied these plumes at high resolution, focusing on the region close to the vent. We examined how the plumes mix with the surrounding water and found that the mixing rate changes significantly with height and time. The results were compared with in situ data and plume theory. Vent temperatures reach 300°C, but anything transported by the plumes would only experience these extreme conditions for very short times. This suggests that hydrothermal plumes may carry biological material, such as larvae, without causing harm. We also studied how vent conditions affect plume behavior, focusing on its transition from the source-dominated region to the turbulent region farther away, where it aligns with the established theory. The transition zone shows behaviors crucial for interpreting seafloor observations. Our findings provide new insights into how hydrothermal plumes behave and interact with deep-sea environments.

1. Introduction

Unlike most of the abyssal plain, hydrothermal fields are oases of life and sites of complex chemistry (Cotte et al., 2020; Van Dover, 2002), where hot fluid is injected from the seafloor into the water column through chimney structures, forming black or white smokers, depending on their chemistry. The steady injection of heat sustains buoyant plumes. These plumes are extreme in many aspects. Their associated heat flux can reach up to $\mathcal{O}(1\ \text{GW m}^{-2})$ (Mittelstaedt et al., 2012), while the average Earth's geothermal heat flux is typically $\mathcal{O}(0.1\ \text{W m}^{-2})$ (Davies & Davies, 2010; Sclater et al., 1980). They can rise a few hundred meters in the weakly stratified deep ocean (Adams & Di Iorio, 2021; Lavelle et al., 2013), while their vent radii are on the order of centimeters. Their temperature at the vent may reach up to ∼400°C, and the injection velocity can be up to ∼1 m s^{-1} (Koschinsky et al., 2008 and Sarrazin et al., 2009). A hydrothermal site is often composed of several edifices, each hosting multiple vents. A hydrothermal plume is therefore a multiscale process, ranging from the scale of the vent, $\mathcal{O}(1\ \text{cm})$, to the scale of the plume height, $\mathcal{O}(100\ \text{m})$. On an even larger scale, hydrothermal plumes are then

transported away laterally by cross-flow circulations, exporting their material over distances of kilometers to hundreds of kilometers.

Most of the oceanographic literature has been devoted to the study of the largest scales of hydrothermal plumes (Speer & Rona, 1989; Thurnherr & Richards, 2001), the influence of Earth's rotation (Fabregat et al., 2016b), their interactions with cross flows (Adams & Di Iorio, 2021; Lavelle et al., 2013), and their lateral dispersion (Vic et al., 2018; Xu et al., 2018). Oceanic buoyant plumes also received a lot of attention after the Deep Water Horizon oil spill in 2010 (Daskiran et al., 2020; Fabregat et al., 2015, 2016a), although the excess buoyancy resulted from the mixture of oil and water rather than heat.

The small scales of hydrothermal plumes, namely from the chimney vent to a few meters, have received much less attention so far. Better knowledge of this near-field zone is important to retrieve the heat flux from in situ measurements (Barreyre et al., 2012; Mittelstaedt et al., 2012), to better assess the temperature fluctuations that control life conditions for faunal assemblages (Girard et al., 2020) and the kinetics of ion precipitation (Chavagnac et al., 2018) and to determine whether larvae may encounter lethal temperatures when vertically transported by the plume (Kim et al., 1994; Mullineaux & France, 1995). To better characterize the hydrodynamics at these scales, in situ measurements are key, but they are challenging to acquire. Only recent developments in acoustic imaging have efficiently captured hydrothermal system properties (Bemis et al., 2015; Xu et al., 2013). Moreover, observations alone are not enough because the turbulence generated by the plumes yields large near-field spatiotemporal fluctuations, both in temperature and velocity, which are difficult to sample with today's instruments and also impact measurements. Observations must be complemented with theory and numerical models.

The main theory is due to Morton et al. (1956), who established a simplified theoretical model of plume dynamics that successfully describes convective plumes in many situations (Kaye, 2008; Woods, 2010). The model describes the averaged properties of the plume along its axis. The model parameterizes turbulence with an entrainment rate parameter α, which relates the lateral entrainment of surrounding fluid into the plume to the plume's axial vertical velocity. The model provides a baseline estimate of averaged properties. Dimensionless studies outside the hydrothermal regime, using direct numerical simulation (DNS) by Marjanovic et al. (2017), Plourde et al. (2008), and Taub et al. (2015) and large-eddy simulation (LES) by Devenish et al. (2010), have demonstrated that the classical assumptions of the theoretical model do not hold in the near-field. In particular, forced or lazy plumes with initial buoyancy transition to a purely buoyant—pure plume—regime (Van Reeuwijk & Craske, 2015). The adjustment between the near-field and far-field hinders the application of theoretical models (Ciriello & Hunt, 2020) and has been poorly characterized for plumes, with even less attention given to the hydrothermal regime.

Despite the importance of buoyant plumes in hydrothermal fields, few numerical studies achieve resolutions that capture the physical processes at the scale of individual vents. Most studies investigate plumes at much larger scales, assuming that the hot fluid has already mixed with the environment and approximating the merging of vent fields (Adams & Di Iorio, 2021; Gao et al., 2019; Lavelle et al., 2013; Tao et al., 2013). This is largely due to the computational cost of achieving vent-scale resolution. Jiang and Breier (2014), however, approached this level of detail using Reynolds-averaged Navier-Stokes simulations, and showed that near-vent dynamics involve complex mixing processes.

Therefore, the hydrothermal plume in the immediate vicinity of chimneys, where most of the temperature gradient occurs, is largely unknown in its details. Key questions are as follows: Does the theoretical model provide a sufficient estimate of the mean conditions? How accurate is the assumption of a uniform entrainment rate? What is the range of temperature fluctuations at a given altitude above the source?

The aim of this paper is to answer these questions using a set of realistic LES, specifically in the hydrothermal regime. We focus on the near-vent region, which represents the window for in situ operations and where smokers interact with biochemical processes. This makes the results directly applicable to the scale of hydrothermal fields.

To address the near-vent physics of buoyant plumes with adequate resolution, we use an LES approach with adaptive mesh refinement (AMR), which allows centimeter-scale resolution within a 6-m domain above the vent. Specifically, we extensively study conditions encountered at the Lucky Strike hydrothermal vent field (northern Mid-Atlantic Ridge), providing a realistic case study. We show that the assumption of a uniform entrainment rate is inaccurate, limiting the use of theoretical model in the near-field. Instead, the LES reveals a systematic

transition region, typically within the first two meters, where the entrainment rate varies, regardless of vent characteristics, and above which the plume enters the pure plume regime. However, in this regime, above the transition region, we find that the mean buoyancy and the mean vertical velocity obey Morton's scaling law. Using the probability distribution of temperatures, we show that although lethal temperatures above 40°C can be found up to 2 m above the source, larvae injected into the plume have a significant chance of experiencing these temperatures for less than a second, supporting the possibility of further transport in the water column.

The paper is organized as follows. Section 2 presents the governing equations and details of the numerical experimental setup. Section 3 investigates the turbulent field of a typical black smoker through its flow structure and compares it with the theoretical model of Morton et al. (1956) and in situ measurements. Section 4 extends the results to a wide range of source parameters to examine the flow field from forced to lazy plume regimes. Section 5 discusses the impact of the transition regime on in situ observations and the effect of temperature fluctuations on biotracer proxies. A summary of the results is given in Section 6.

2. Model and Numerics

2.1. Plume Theory

The theory established by Morton et al. (1956) describes an axisymmetric Boussinesq plume with a radius r in a stratified fluid, with the assumption that the radial profiles of vertical velocity w and buoyancy b are similar at all heights z (i.e., the vertical coordinate). This model is hereafter referred to as the MTT model. This approach relies on the entrainment rate α, a parameterization of mixing, which relates w at each height to the radial velocity e of the entrained water in the plume, such that $\alpha = e/w$.

The conservation of volume, momentum, and buoyancy flux, under these assumptions, yields the following equations:

$$\frac{d}{dz}\left(r^2 w\right) = 2\alpha r w, \tag{1a}$$

$$\frac{d}{dz}\left(r^2 w^2\right) = 2r^2 b, \tag{1b}$$

$$\frac{d}{dz}\left(r^2 w b\right) = 2r^2 w \frac{g}{\rho_r}\frac{\partial \rho_a}{\partial z}, \tag{1c}$$

where ρ_a represents the ambient fluid density, ρ_r is a reference density, and g is the gravitational acceleration. In this model, $b = -g\left(\rho_p - \rho_a\right)/\rho_r$, where ρ_p is the plume density.

From the solutions of Equations 1a–1c, the neutral buoyancy level H_{nbl} and the maximum height due to momentum overshoot H_{top} can be estimated as follows (Devenish et al., 2010):

$$H_{nbl} = 1.04\,\alpha^{-1/2} B_0^{1/4} N^{-3/4}, \tag{2a}$$

$$H_{top} = 1.36\,\alpha^{-1/2} B_0^{1/4} N^{-3/4}, \tag{2b}$$

where N is the buoyancy frequency, and $B_0 = \pi r_0^2 w_0 b_0$ is the buoyancy flux at the source, with $z = 0$ denoted by the subscript 0. The momentum flux and vertical volume flow are defined as $M_0 = \pi r_0^2 w_0^2$ and $Q_0 = \pi r_0^2 w_0$, respectively.

In most cases, hydrothermal plumes carry momentum from the source, induced by subseafloor pressure. Morton and Middleton (1973) introduced two dimensionless parameters to characterize the balance of forces, expressed as

$$\Gamma(z) = \frac{r(z) b(z)}{\alpha w(z)^2}, \tag{3a}$$

$$\Gamma(z)' = \frac{\alpha b(z)}{r(z)N^2}. \tag{3b}$$

At $z = 0$, Γ_0 and Γ_0' represent the plume source parameters. For $\Gamma_0 < 1$, the plumes are forced (relative excess of momentum), and for $\Gamma_0 > 1$, the plumes are lazy (relative excess of buoyancy). When $\Gamma_0' \ll 1$, the plume is rapidly balanced by the ambient stratification. The a priori choice of α affects the Γ_0 level and plume classification near $\Gamma_0 = 1$. Taub et al. (2015) noted that this dependence can cause inconsistencies between theory and observations.

The value of α remains a subject of debate. The generally accepted values are 0.12 for buoyant plumes and 0.076 for pure jets (Kaye, 2008; Richardson & Hunt, 2022; Van Reeuwijk & Craske, 2015; Woods, 2010). However, recent studies show that α can vary greatly in the near-field (Marjanovic et al., 2017; Van Reeuwijk et al., 2016). We assume a fixed value of $\alpha = 0.12$ for application to Equations 1a–1c, 2a, 2b, 3a, and 3b.

2.2. Basilisk

Basilisk (Popinet, 2013) is an AMR code that uses an octree structure to discretize the computational domain. This approach provides refined resolution in regions with small-scale features, while coarsening the grid in quiescent areas. The dynamic refinement adapts the mesh on the fly, efficiently focusing computational effort on turbulent regions, making it well suited for plume studies. The code uses an LES approach with a second-order accurate finite-volume solver for the Navier-Stokes equations (Popinet, 2003, 2009, 2015). The equations are solved using the Boussinesq and incompressibility assumptions, expressed as

$$\frac{\partial \mathbf{u}}{\partial t} + \nabla \cdot (\mathbf{u} \otimes \mathbf{u}) = \frac{1}{\rho_r}(-\nabla p + \nabla \cdot \mathbf{T}) + b\nabla z, \tag{4a}$$

$$\nabla \cdot \mathbf{u} = 0, \tag{4b}$$

$$\frac{\partial T}{\partial t} + \nabla \cdot (\mathbf{u}\, T) = -\nabla \cdot \mathbf{J}, \tag{4c}$$

where $\mathbf{u}$ is the filtered velocity, T is the filtered temperature, and z is the height above the source. The buoyancy is defined as $b = -g(\rho(x,t) - \rho_r)/\rho_r$, where $\rho(x,t)$ is the density at position x and time t, and $\rho_r = 1\,035\ \mathrm{kg\ m^{-3}}$ is the reference Boussinesq density. The model pressure p, representing the deviation from the hydrostatic reference pressure P, is computed using a multigrid Poisson solver. The density is computed by an extension of the equation of state (EOS) beyond the oceanic funnel, namely for $T > 40$°C (see below). The stress tensor $\mathbf{T}_{ij} = 2(\nu_e + \nu_m)\, s_{ij}$ accounts for unresolved small-scale turbulence, with $s_{ij} = (\alpha_{ij} + \alpha_{ji})/2$ the deformation rate, $\alpha_{ij} = \partial u_j/\partial x_i$, ν_m the molecular viscosity, and ν_e the eddy viscosity. The Vreman (2004) subgrid scale model is used to compute the local eddy viscosity $\nu_e = cB_\beta^{1/2}/(\alpha_{ij}\alpha_{ij})^{1/2}$, with $B_\beta = \beta_{11}\beta_{22} + \beta_{22}\beta_{33} + \beta_{33}\beta_{11} - \beta_{12}^2 - \beta_{23}^2 - \beta_{13}^2$ and $\beta_{ij} = \Delta^2\alpha_{ki}\alpha_{kj}$ and Δ as the local grid width. The model coefficient c is set to 3.6×10^{-2}, to allow a fair chance for turbulent shear flow. The temperature T is integrated as a conservative tracer using the robust upwind advection scheme of Bell et al. (1989). The diffusive flux $\mathbf{J} = -(K_e + K_m)\nabla T$ includes the molecular diffusivity K_m and the eddy diffusivity K_e, which we set equal to the eddy viscosity, that is, $K_e = \nu_e$. The viscous dissipation ε_k is diagnosed as $\varepsilon_k = 2(\nu_e + \nu_m)\, s_{ij}s_{ij}$ (see Section 4.1 for details).

The Boussinesq approximation may seem questionable due to the large temperature anomalies at the vent, where the source temperature in this study is typically around $T_0 = 300$°C ($\rho_0 = 782\ \mathrm{kg\ m^{-3}}$) and the ambient temperature is $T_a = 4.6$°C ($\rho_a = 1035\ \mathrm{kg\ m^{-3}}$). However, the plume mixes rapidly as it exits (see Section 3). At 25 cm above the source, the average temperature drops to $T = 50$°C ($\rho = 1021\ \mathrm{kg\,m^{-3}}$), corresponding to an average density fluctuation of 1.4% with respect to the reference density. At $z = 1$ m, the mean temperature is close to $T = 10$°C, corresponding to a fluctuation of 1%, and temperatures of $T > 40$°C ($\rho < 1025\ \mathrm{kg\,m^{-3}}$) make up only 40% of the distribution (Figure 2e). Furthermore, the buoyancy flux is preserved in this approximation. Thus, the introduced error is not expected to have a significant effect on our results.

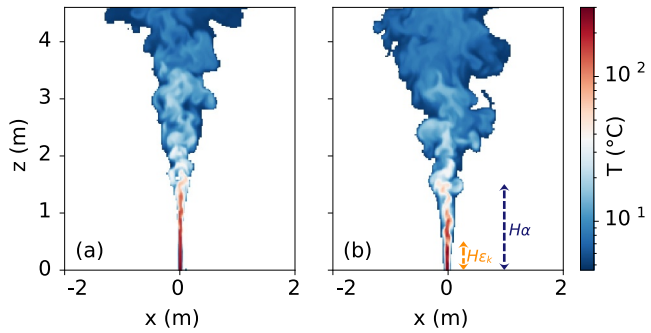

Figure 1. Cross-section of the instantaneous temperature field from Experiment 1, for (a) the scenario without noise perturbation at the outlet ($A = 0$) and (b) with turbulence triggered by noise immediately after the outlet ($A = 0.5$). The two reported heights correspond to the transition region to a pure plume regime (see Section 4).

2.3. Equation of State

An accurate EOS is needed for the 4–300°C temperature range, at the hydrostatic pressure of our target site, which is $P \sim 1700$ dbar. TEOS-10 (IOC et al., 2010) is the standard for computing seawater thermodynamics but is only valid in the oceanic funnel, that is, $T < 40$°C at 2,000 m (McDougall et al., 2003). We need to extend the EOS for temperatures above this range. Previous work by Sun et al. (2008) established a set of fitted polynomial equations in the 4–300°C range by combining freshwater and seawater data. A more recent study by Safarov et al. (2009), based on in situ measurements at $S_A = 35.17\,\mathrm{g\,kg^{-1}}$, covers the entire 0–195°C range up to 1,400 dbar with improved accuracy. Bischoff and Rosenbauer (1985) determined the EOS for $S_A = 32.16\,\mathrm{g\,kg^{-1}}$ for the 200–350°C range and up to 1,000 dbar. To simplify the model and due to a lack of sufficient data, we neglect the specific chemistry of black smokers and assume a uniform absolute salinity of $S_A = 35.2\,\mathrm{g\,kg^{-1}}$. To develop a smooth EOS that closely matches these published results, we developed a nonlinear parametric fit covering the temperature and pressure range 0–350°C and 1500–1700 dbar, typical of the conditions at Lucky Strike (Figure A1). To balance the salinity differences, the data from Sun et al. (2008) and Bischoff and Rosenbauer (1985) are adjusted based on TEOS-10 at $S_A = 35.2\,\mathrm{g\,kg^{-1}}$. The corresponding correlation is given in Appendix A by Equation A1.

2.4. Outlet Turbulence Parameterization

The discrete sources observed at Lucky Strike systematically exhibit turbulence at the vent, which is expected due to the complex and irregular subsurface circulation that hot fluids undergo before reaching the seafloor (Fontaine et al., 2014). However, without numerical adjustments, the plume initially develops as a transitional laminar flow (Figure 1a) until it destabilizes into a turbulent plume. This is an unrealistic feature that is corrected using the method of Plourde et al. (2008). To trigger turbulence in the plume, a uniform discrete white noise signal $W(t) \in [-1, 1]$ is added to the vertical velocity at all outlet nodes (Figure 1b, Experiment 1 in Table 1), such that $w = w_0(1 + AW(t))$, where A is the noise amplitude. This parameterization represents the turbulence pre-existing in the flow prior to injection into the water column and fully accounts for the turbulent state at the outlet. The calculations show that for disturbance magnitudes $A = [0–2]$, the level of turbulence can be increased while keeping the plume numerically stable. However, a burst of ε_k in the first nodes above the outlet limits the maximum energy that can be injected at the source. Therefore, we choose the optimal value of $A = 0.5$, which allows turbulence to develop quickly after the outlet while minimizing the burst in ε_k.

Table 1
Summary of Simulations

Experiment	Symbol	w_0 (m s^{-1})	r_0 (cm)	T_0 (°C)	b_0 (m s^{-2})	B_0 (m^4 s^{-3})	Γ_0
1, 2, and 3	■, ⬟, ◆	0.7	2.8	[300, 100, 200]	[2.4, 4.1e−1, 1.2]	[4.1e−3, 7.1e−4, 2.1e−3]	[1.1, 0.2, 0.6]
4, 5, and 6	✚, ✖, |	[1.4, 0.7, 0.35]	[1.4, 2.0, 2.8]	300	2.4	2.1e−3	[0.1, 0.8, 4.6]
7 and 8	×, ▶	[1.4, 0.05]	2.8	300	2.4	[8.3e−3, 3.0e−4]	[0.3, 224]
9, 10, and 11	★, ⬢, ◀	0.5	[1.4, 2.0, 2.8]	300	2.4	[7.4e−4, 1.5e−3, 3.0e−3]	[1.1, 1.6, 2.2]
12 and 13	◆, ⬣	[0.05, 0.2]	1.4	300	2.4	[7.4e−5, 3.0e−4]	[112, 7.0]
14 and 15	▲, ⬣	[0.05, 1.4]	2.8	40	9.2e−2	[1.1e−5, 3.2e−4]	[8.5, 0.01]
16 and 17	_, ✶	[0.05, 1.12]	[1.4, 2.8]	200	1.2	[3.7e−5, 3.3e−3]	[58, 0.23]
18	▼	0.02	2.8	340	3.3	1.6e−4	1897

Note. The experiments are grouped based on common varying factors. The numerical domain size is $L_0 = 6.375$ m. The maximum resolution is the same across all simulations ($\Delta_{max} = 2.49$ cm).

2.5. Experiment Setup and Modeling Case

The Tour Eiffel vent field (−1690 m) located at the Lucky Strike hydrothermal site (37°17′N, 32°16′W) is selected as the baseline modeling case. It features a prominent 15-m high chimney with approximately 10 vents (Mittelstaedt et al., 2012) and is considered a biological hotspot (Van Audenhaege et al., 2022). We define a hydrothermal edifice as the collection of chimneys and complex topography resulting from hydrothermal activity. Usual structures are smaller than Tour Eiffel, typically ∼1–2 m in height (Barreyre et al., 2014).

Hydrothermal fluid exits the seafloor through two types of sources: diffuse low-temperature sources ($T < 10$°C), which are a mixture of hydrothermal fluid and ambient water, and discrete high-temperature sources, typically black smokers (Barreyre et al., 2014). We focus on the plumes emitted by the latter. The EMSO (European Multidisciplinary Subsea Observatory)-Açores long-term observatory, maintained through the MoMARSAT campaign series, provides the framework for in situ measurements.

The model domain is a cubic box of width $L_0 = 6.375$ m. We set the maximum level of refinement to eight so that the maximum resolution is $\Delta_{\max} = L_0/2^8 = 2.49$ cm to spatially resolve the vent outlet, while the minimum level of refinement is set to five, corresponding to a minimum resolution of $\Delta_{\min} = L_0/2^5 = 20$ cm. We use open boundary conditions on all sides, except for a solid flat bottom. To avoid boundary effects, results are presented excluding regions near the boundaries. The plume is forced by imposing a temperature T_0 and vertical velocity w_0 at the vent, modeled as an outlet with radius r_0. A solid pipe was tested as a small chimney model in order to raise the outlet 1 m above the seafloor and thus enable more effective entrainment of the surrounding fluid. Simulation results showed no significant differences, so for simplicity, the outlet is kept at the bottom boundary. The ambient stratification is linear in the vertical, with $N = 1.63 \times 10^{-3}$ s^{-1}, determined from observations at Lucky Strike. The ambient temperature at the outlet is $T_a = 4.6$°C.

The diversity of source conditions is large, ranging from highly forced plumes to highly lazy plumes. To capture this variability, the study examines a number of key parameters: r_0 (1.4–2.8 cm), w_0 (0.02–1.4 m s^{-1}), and T_0 (40–340°C). In practice, the sources are represented by one, two, or four grid points at the maximum resolution $\Delta_{\max}$. The source radius r_0 corresponds to that of a disc having an identical surface area. The selected range for these parameters is based on field data collected by Mittelstaedt et al. (2012) at Tour Eiffel. The experimental parameters are summarized in Table 1.

2.6. Averaged Diagnostics

To synthesize the LES results, diagnostic quantities are averaged both in time and horizontally to provide vertical profiles. Horizontal averaging is performed within the plume, which requires the definition of the plume boundary relative to the ambient. This definition is not straightforward, and there is no generally accepted approach in the literature. Few attempts have been made to provide a precise definition (Pham et al., 2005; Plourde et al., 2008).

In this study, we define the plume boundary based on w; the plume interior is where $|w| > \sigma$. The typical value used is $\sigma = 10^{-2}$ m s^{-1}, determined by sensitivity tests, with any deviations specified. This criterion filters velocities between 1% and 10% of the axial values and is consistent with Morton et al. (1956)'s definition of the theoretical plume radius. We have verified that this criterion accurately captures the plume boundary for all source parameters in this study.

We define $r(z,t)$ as the equivalent radius of the area $S(z,t)$, where $S(z,t)$ is the plume cross-sectional area used for horizontal averaging. On average, $S(z,t)$ corresponds to a disc, but this is not true for snapshot times, as turbulence causes the plume boundary to become convoluted. The profiles are time-averaged over the integration time (∼10 min plume time) with an output every 1.5 s.

The entrainment rate is a key quantity from the LES and is obtained by $\alpha(z,t) = e(z,t)/w(z,t)$, where $e(z,t)$ is the lateral flux entering the plume and $w(z,t)$ is the mean vertical velocity. It is computed using

$$e(z,t) = \frac{1}{2\pi r(z,t)} \frac{d}{dz}(wS), \tag{5a}$$

$$w(z,t) = \frac{1}{S(z,t)} \int_{S(z,t)} w \, dS. \tag{5b}$$

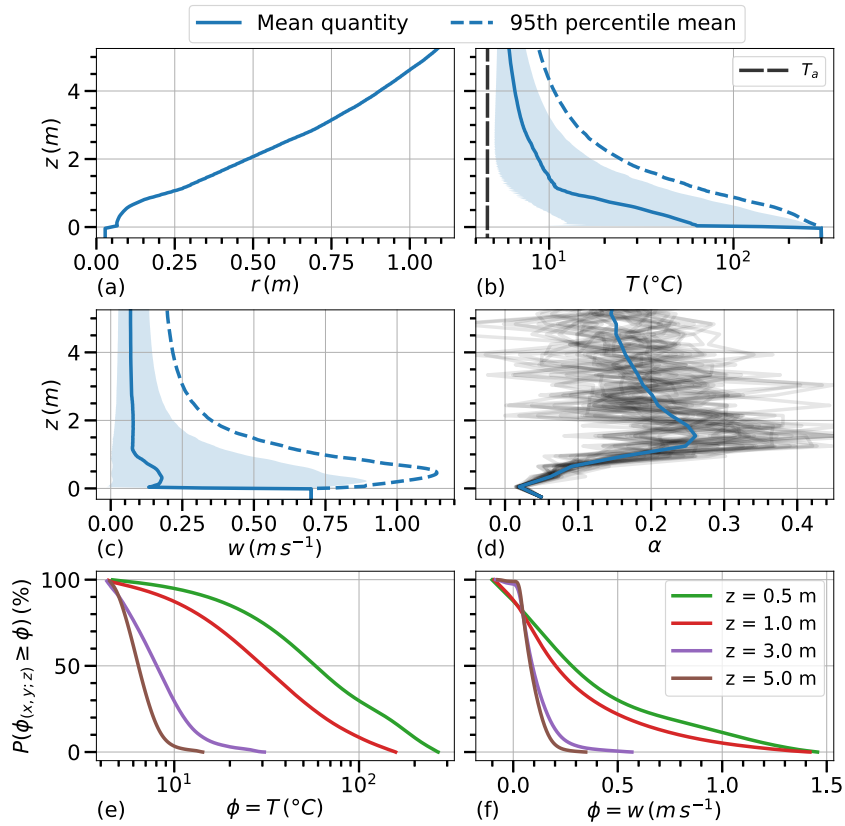

Figure 2. Vertical profiles from Experiment 1 of the time-averaged (a) radius, (b) temperature, and (c) vertical velocity. (b) T_a is the ambient temperature (4.6°c). The dashed line represents the 95th percentile mean (core plume), and the shaded region indicates the asymmetric spatial standard deviation. (d) Evolution of the entrainment rate $\alpha(z)$ and its temporal variability. Complementary cumulative density function for (e) temperature and (f) vertical velocity at different heights above the source.

3. Model Result for a Black Smoker

The aim of this section is to describe the near-field plume dynamics, to investigate the flow structure as a function of the entrainment rate, and to compare these results with those predicted by the MTT theoretical model and in situ data.

3.1. Mean Field

The experiment presented here represents a typical source at the Lucky Strike field (Experiment 1 of Table 1). The regime is weakly lazy ($\Gamma_0 = 1.14$), and as noted in Section 2.1, the choice of α affects the value of Γ_0. Its turbulent flow is more similar to a forced plume regime (see Section 3.3), and the term forced plume is used for Experiment 1. We present the mean quantities averaged with $\sigma = 1$ cm s^{-1} in Figure 2, together with the 95th percentile mean to highlight the upper range of the data distribution. Positive and negative spatial standard deviations are shown separately.

The high value of $\Gamma'_0 = 4 \times 10^6$ reflects the strong injection of B_0 into a weak stratification. The plume exits with an extremely high temperature anomaly ($T - T_a \approx 300$°C) and intense momentum forcing ($w_0^2 = 0.5$ m^2 s^{-2}), significantly different from typical ocean conditions. It results in $H_{nbl} \approx 3400\, r_0$ according to the MTT model (see below), underscoring the focus on near-field behavior within this study ($L_0 \approx 230\, r_0$). However, the plume quickly converges to a more tempered state within the numerical domain, typical of the scale of hydrothermal edifices.

The mean temperature drops sharply from $T_0 = 300$°C at the vent to less than $T = 6.5$°C at $z = 4$ m and then follows a slower decay rate (Figure 2b). Within the first meter, the temperature drops below $T = 15$°C. Despite

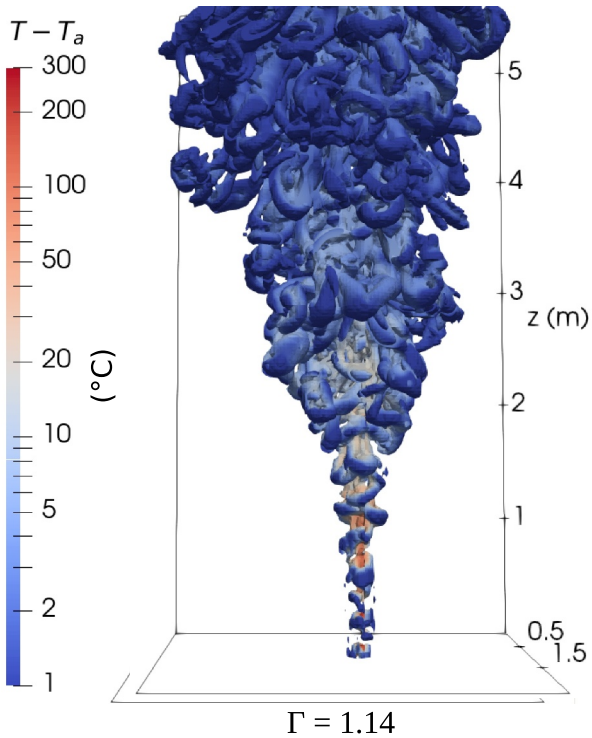

Figure 3. Three-dimensional coherent structures are visualized using the λ_2 method (Jeong & Hussain, 1995) for iso-surfaces at $\lambda_2 = -0.1$ for a plume near the forced plume regime (Experiment 1). The colormap represents the temperature anomaly, with $T_a = 4.6$°C.

this rapid decrease, the region near the vent retains significantly high mean temperatures. The mean vertical velocity goes from $w_0 = 70$ cm s^{-1} to $w = 7$ cm s^{-1} within the first meter (Figure 2c). w remains almost constant above this, with only a 10% variation between $z = 1$ m and $z = 5$ m. The first meter is characterized by fluid acceleration, with the plume core reaching a peak velocity of $w = 1.14$ m s^{-1} at $z = 0.5$ m, as discussed further below. The radius increases linearly, indicating a constant spreading rate, reaching $r = 1.05$ m at $z = 5$ m. The area of averaging includes the boundary of the plume where most of the mixing occurs. The averages are therefore sensitive to these regions of very low values, which contribute to the sharp decreases in key variables and the rapid expansion observed immediately after the outlet in Figure 2a.

The plume dynamics observed in Figure 2, notably the stabilization of T and w profiles to nearly constant values, represent the adjustment between the near-field and far-field regions. The entrainment of ambient water is necessary to dissipate the large values of T_0 and w_0 through mixing. This is reflected in the rapid increase in the radius, which grows by a factor of 37 between the vent and a height of $z = 5$ m. This can be considered the dilution factor of the hydrothermal fluid (Figure 2a). Coupled with the vertical velocity, this results in a significant volume flow of $Q = 0.25$ m^3 s^{-1} at $z = 5$ m. Thus, Q grows by a factor of 145 over a height of $z \approx 200\, r_0$, highlighting the efficiency of buoyancy-driven entrainment.

The weak stratification has no significant effect in the near-field. It was included in the LES setup to make the simulation more realistic and to avoid unnecessary assumptions about the surrounding fluid. However, LES runs under the same conditions as Experiment 1, but with a uniform ambient, gives identical results for the vertical profiles of the mean quantities. Nevertheless, the parameter N is crucial for explaining the plume equilibrium level and cannot be ignored in larger numerical domains. According to the MTT model, the neutral buoyancy level and maximum height are predicted to be $H_{nbl} = 94$ m and $H_{top} = 123$ m, respectively (Equations 2a and 2b). The solution of the MTT equations in uniform versus stratified environments begins to diverge at $z \approx 0.4H_{nbl}$. Here, the numerical domain represents $0.07H_{nbl}$, which seems to be a reasonable limit for assuming a uniform environment, without accumulating significant errors.

3.2. Spatial Fluctuations

The rapid drop in mean temperature does not mean that the hot water is immediately and completely mixed. Mixing takes some time. The 95th percentile distribution is assumed to represent the core of the plume. In this region, the temperature is significantly higher than that at the plume's edge (Figure 2b), where ambient cold water is drawn in and subsequently mixed.

To understand the mixing process, we present the complementary cumulative density function (CCDF) for temperature at different heights above the source (Figure 2e). The CCDF shows the probability of finding a parcel at height z with a temperature greater than T. For example, at $z = 1$ m, 50% of the parcels have temperatures above 30°C, and 10% exceed 100°C, while the mean temperature is only 10°C. This provides information beyond the predictions of the MTT model and is valuable for understanding chemical processes and larval dispersal. Implications for biological particles are discussed in Section 5.2. At $z = 3$ m, the maximum observed temperature is 30°C.

We apply the same diagnostic to the vertical velocity (Figure 2f). Two points stand out. First, local velocities can reach up to twice the exit velocity (up to 1.5 m s^{-1}) below $z = 1$ m. Second, downward velocities occur within the plume, although with low probability. The latter is directly related to the twisting vortical structures and their associated circulations (Figure 3). The first property shows that the core of the plume is being accelerated. This acceleration is driven by buoyancy, with the available potential energy carried by the hot water acting as a source

of kinetic energy (Winters et al., 1995; Wykes et al., 2015). Figure 2c clearly shows that the vent buoyancy provides a local acceleration of the core plume, strong enough to influence the mean value. The fluid acceleration means that any in situ measurement must take this effect into account, as estimating the vent volume flow just centimeters above the source could lead to significant errors.

The distribution of large anomalies in T and w remains significant within the first meter. Due to the high temperature of the core being mixed, a specific extension of the TEOS-10 EOS is still required 1 m above the vent. This highlights that the assumption of a homogenized fluid based on mean quantities, with low w and T values for $z < 3$ m, is incorrect. However, mixing drastically changes the balance of forces, subsequently slowing the vertical motion and reducing the variance in the plume quantities w and T. Beyond this region ($z > 3$ m), the distributions of T and w show reduced spatial variation, which explains the slower decrease of their profiles and their convergence to nearly constant values. At $z = 5$ m, the absolute spread of T and w decreases to 10°C and 0.34 m s^{-1}, with a lower probability of extreme values than an absolute spread of 155°C and 1.4 m s^{-1} at $z = 1$ m.

A key result is that the flow structure must be carefully considered in experiments that initiate simulations at a dilute point above the vent, as many hydrothermal plume simulations rely on this approach (Adams & Di Iorio, 2021; Gao et al., 2019; Lavelle et al., 2013). Approximating a uniform source below $z = 5$ m fails to capture the dynamics of the near-vent flow structure. In particular, the velocity fluctuations indicate that turbulence is fully developed, and the plume cannot be assumed to be laminar in the near-field.

3.3. Entrainment and Flow Structure

The entrainment rate, $\alpha(z,t)$, shows strong vertical and temporal variability, associated with intense mixing and the plume dilution. The overall value in the domain is $\alpha = 0.19$, but it shows a vertical dependence with three distinct zones, consistent with previous results obtained using DNS by Van Reeuwijk et al. (2016). For $z < 0.7$ m, the forced plume is driven by the source condition. The entrainment rate is similar to that of a jet-like plume, $\alpha = 0.07$. This region corresponds to most in situ observation capabilities. In the range 1 m $< z < 2$ m, the entrainment rate reaches its maximum ($\alpha = 0.26$), which is twice the commonly accepted value for buoyant plumes. This entrainment rate reflects intense mixing with cold fluid, contributing to the plume spreading, as well as the dilution and homogenization of the temperature anomaly distribution. Buoyancy driving the flow weakens, resulting in deceleration. For $z > 3$ m, the entrainment rate converges to a more conventional value ($\alpha = 0.15$) for a pure plume (Richardson & Hunt, 2022; Van Reeuwijk & Craske, 2015). This suggests that the plume reaches a self-similar state, marking the end of the near-field transition regime (discussed in more detail in Section 4). This transition, as previously noted, is associated with an abrupt change in the key variables T and w for $z > 2$ m, with both converging to a weaker vertical decay rate (Figures 2b and 2c). The dilution process is responsible for the dissipation of the large buoyancy flux B_0 at the source.

The $\alpha(z)$ profile is closely related to the turbulence field, which consists of different scales of coherent structures. These structures can be observed using the λ_2 technique (Jeong & Hussain, 1995), as shown in Figure 3. A real-time sequence of the turbulent field observed with this technique is provided by the authors (Lemaréchal et al., 2024a). The jet-like entrainment rate close to the source ($z < 0.7$ m) is associated with an unstable shear layer that forms ring vortices along the plume axis, typical of jet-like flow. As the entrainment rate increases with height ($z < 1.5$ m), the flow field becomes turbulent. The vortices destabilize and break down into a helical mode, as described by Fiedler (1988). The large, well-organized vortex structures between 1 and 2 m, predominantly aligned in the horizontal plane, entrain more fluid than the smaller, less organized vortices that appear further downstream. This explains the maximum value of $\alpha(z)$ observed at this height. This marks the transition region, where both the kinetic energy dissipation and the entrainment rate reach their peak. Beyond $z = 1.5$ m, the entrainment rate decreases as the flow enters a fully 3D convective turbulent state (pure plume). The plume structure directly influences the entrainment rate and the energy dissipation dynamics.

The instantaneous entrainment rate profiles (Figure 2d—black lines) show significant temporal variability. $\alpha(z,t)$ reaches a value of 0.5 at $z = 1.6$ m, representing a 90% deviation from the mean. This observation adds to the evidence for strong mixing in the vicinity of the vent. Similar behavior has been observed in experimental studies (Matulka et al., 2014) and DNS studies (Marjanovic et al., 2017; Plourde et al., 2008). We observe the same pattern in the hydrothermal regime. The temporal variability results from large-scale vortical structures driving the turbulent flow, as highlighted by Plourde et al. (2008). Most of the entrainment occurs at the plume's edge, while the core remains less sensitive to mixing. Negative entrainment, up to $\alpha = -0.06$, is associated with

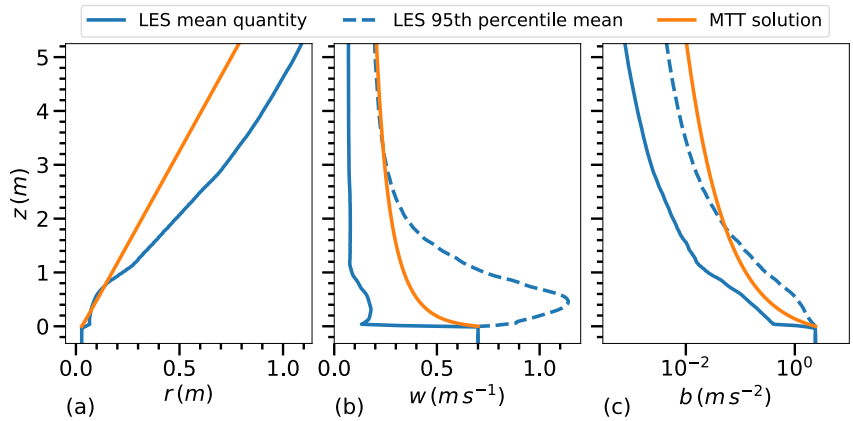

Figure 4. Vertical profiles of the flow field from Experiment 1 compared to the results obtained with the MTT model (1956) for its governing parameters: (a) radius, (b) vertical velocity, and (c) buoyancy. The dashed line represents the 95th percentile mean of the large-eddy simulation results (core plume).

detrainment processes reflected in the local downward velocities. This is associated with the expulsion of fluid from the plume due to coherent turbulent structures. The influence of this mechanism on the mean field becomes noticeable only after $z = 3$ m. Plourde et al. (2008), using higher resolution DNS, identified it as an expulsion and contraction mechanism of local coherent structures driving the dominant entrainment process.

3.4. Comparison With the MTT Model

LES mean quantities can be compared with predictions from integral models. Figure 4 compares LES data with the MTT model predictions, the most widely used theoretical model. It shows that the self-similar conservation equations derived by Morton et al. (1956) do not hold in the near-field. The MTT equations in Figures 4a–4c capture the general trend of the flow field but do not agree well with the mean profiles. This discrepancy cannot be attributed to horizontal averaging choices, as the MTT model best represents the core plume evolution for $z > 2$ m. At $z = 5$ m, the radius predicted by the MTT model is 30% smaller, and the difference in the velocity profiles results in $Q = 0.37$ m^3 s^{-1}, which is 30% higher than the LES flow field.

In particular, the fluid acceleration contradicts the self-similarity assumption in the MTT model, which predicts a monotonic decrease in vertical flow velocity (Figure 4b). This was shown by Marjanovic et al. (2017) for lazy plumes. Here, we show that the buoyancy flux injected by black smokers in a forced plume regime is sufficient to induce the same effect.

A virtual origin correction can be applied to the source to account for the point source assumption of the MTT model (Hunt & Kaye, 2001). However, the length $L_q = 5Q_0/\left(6\alpha M_0^{1/2}\right)$, which represents the distance from the actual source to the virtual source of a pure plume (Hunt & Kaye, 2005), has little effect on the results ($L_q = 29$ cm) and is therefore not applied.

The adjustment between the vent conditions and an ordered far-field flow, corresponding to a pure plume regime, is responsible for the breakdown of the self-similarity assumption. This prevents the direct application of the theoretical model. This is in agreement with recent findings by Ciriello and Hunt (2020), Marjanovic et al. (2017), Matulka et al. (2014), and Van Reeuwijk et al. (2016) and highlights the need for analytical solutions adapted to this region. This adjustment to the far-field occurs through mixing, which is reflected in the strong variability of the $\alpha(z,t)$ profile. Thus, our work confirms the main limitation of the MTT model: the entrainment rate cannot be assumed constant in the transition region between the near-field and far-field. It shows that although theoretical models are often used to calibrate measurement techniques (Crone et al., 2008; Mittelstaedt et al., 2012), near-field hydrothermal plume predictions cannot rely solely on these models.

Another approach to measuring the entrainment rate is to derive α from the spreading rate, represented by the local derivative $\partial z/\partial r$ and expressed as the angle $\hat{\beta}$ between the plume boundary and the horizontal plane. Plumes do not always maintain a constant spreading rate, particularly in cases of necking in lazy plumes (Marjanovic et al., 2017). Here, however, the radius shows a steady increase, corresponding to a nearly constant angle

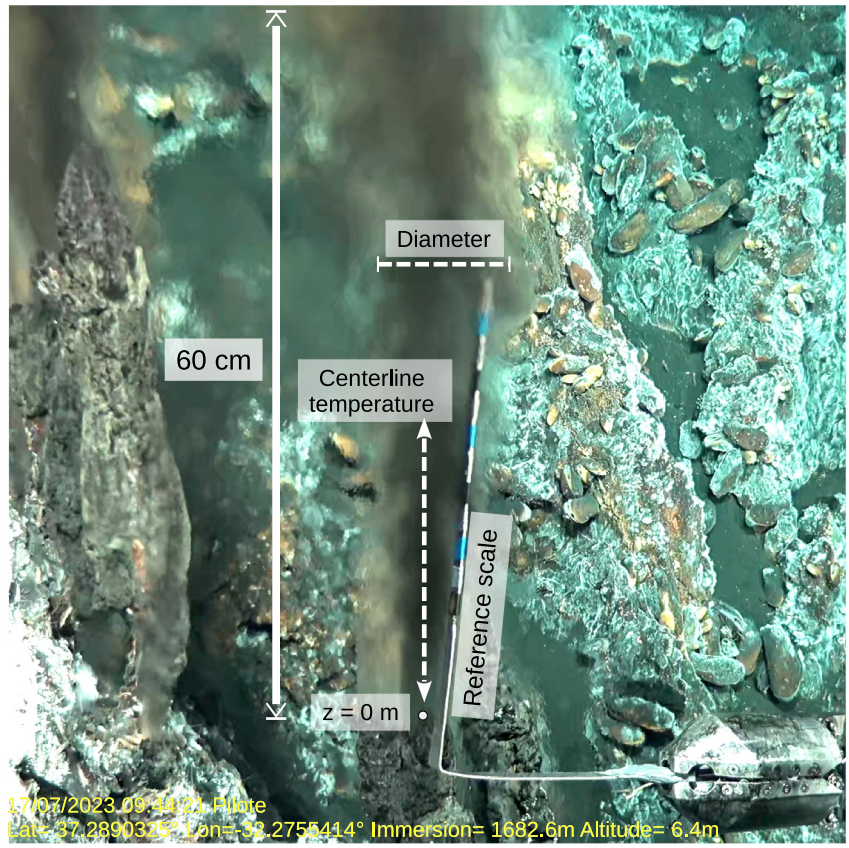

Figure 5. Photograph of the plume and a schematic of the parameters used to measure the temperature and diameter of the plume. The reference scale gives the pixel-to-real distance ratio. Height above the source is measured from the reference point at $z = 0$ m. Diameter is measured by identifying the visible outer edges of the plume relative to the surroundings. Temperature is measured along the centerline of the plume.

$\hat{\beta} = 84°$. The spreading rate is linked to the MTT assumptions through α. Applying $\hat{\beta}$ to the conservation of volume in the MTT model gives a theoretical value of $\alpha = 0.10$.

Two key points can be made. First, the spreading rate remains nearly constant in the near-field for hydrothermal plumes. This is consistent with the assumption of the model developed by Priestley and Ball (1955), which is related to the MTT model (Fox, 1970). Secondly, the derived value of $\alpha = 0.10$ is close to the classical one (Richardson & Hunt, 2022), while the mean value $\alpha = 0.19$, obtained through direct computation, is almost twice as high due to the turbulent field in the near-vent region. This shows that while black smokers can be captured to some extent by integral models, these models fail to reproduce the detailed dynamics observed near the vent.

3.5. Comparison to In Situ Observations

Here, we assess how accurate our model is compared to direct measurements. Reproducing black smokers in laboratory experiments is technically challenging (Crone et al., 2008; Shabbir & George, 1994), while accessing hydrothermal fields at depth presents its own set of challenges. Our LES results are compared with in situ data from the MoMARSAT2023 cruise using remotely operated vehicle (ROV) operations.

The in situ experimental setup is shown in Figure 5. Sampling was performed at a typical source in the Tour Eiffel field. The vertical observation window, H_{obs}, is limited to 60 cm above the vent. The key parameters to be retrieved are the plume radius and the temperature profile. The optical width, that is, the visible gradient density anomalies, provides a measure of the apparent radius of the plume, although this measure is subject to perspective distortion. Radius measurements are based on video recordings with a reference scale, consisting of 300 frames and a step size of $dz_{obs} \approx 5\% H_{obs}$. The temperature profile is measured with a probe positioned along the plume

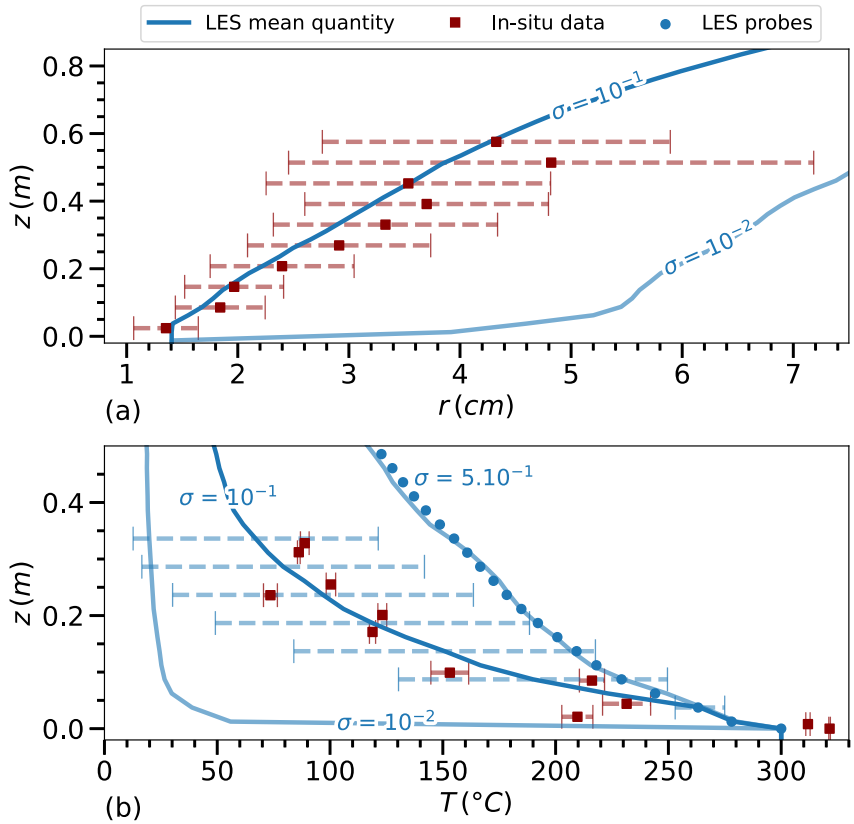

Figure 6. Profiles of (a) the plume radius and (b) temperature for the in situ data and the large-eddy simulation (LES) mean quantities (Experiment 9) for different values of σ (in m s^{-1}). The blue dots represent numerical probes indicating the time-averaged temperature at the plume axis. The error bars represent the spatial root mean squared (RMS) for the LES data and the temporal RMS for the in situ data.

centerline above the vent, with $dz_{obs} \approx 10\% H_{obs}$ and a sampling rate of 1 Hz. Horizontal currents were negligible during the experiment.

The in situ data are compared with the LES equivalent in Figure 6 (Experiment 9 of Table 1). The values of $r_0 = 1.4$ cm and $T_0 = 300$°C for the LES experiment are chosen based on the in situ measurements at $z = 0$ m. The root mean squared (RMS) value is used to represent the temporal dispersion of the in situ data.

The vertical velocity at the source is a complicated parameter to measure accurately using only video data (Crone et al., 2008; Mittelstaedt et al., 2012). First, σ is set to 10 cm s^{-1}, which captures the plume contour effectively measurable in videos. For any given set of source parameters tested, a smaller σ value includes density gradients too weak to be detected visually in the video, as well as colder parcels. This causes an incoherent sharp increase and decrease in r and T, respectively, immediately after the exit (Figures 6a and 6b). Then, w_0 is estimated based on LES experiments. Several experiments are run with the same r_0 and T_0 values as above, to determine the w_0 value that gives a radius and the temperature profile that best matches the in situ data. It is found to be $w_0 = 0.5$ m s^{-1}.

The LES radius and temperature profiles are in good agreement with the experimental data. The variability of the in situ radius at z_0 reflects the temporal evolution of the effective equivalent surface through which the flow passes. In fact, the vent geometry does not resemble a well-defined pipe but consists of closely spaced sources, each less than a centimeter wide, which together form a single plume exit. The RMS of the in situ data increases with height as the plume moves and bends away from its axis, introducing a bias from the 2D view of the apparent radius, which is not captured by the LES method of calculating r.

The LES plume is slightly colder at the source, but this does not significantly affect the profiles. The LES experiment accurately reproduces the rapid decrease from 220°C at $z = 5$ cm to 85°C at $z = 30$ cm. The blue dots

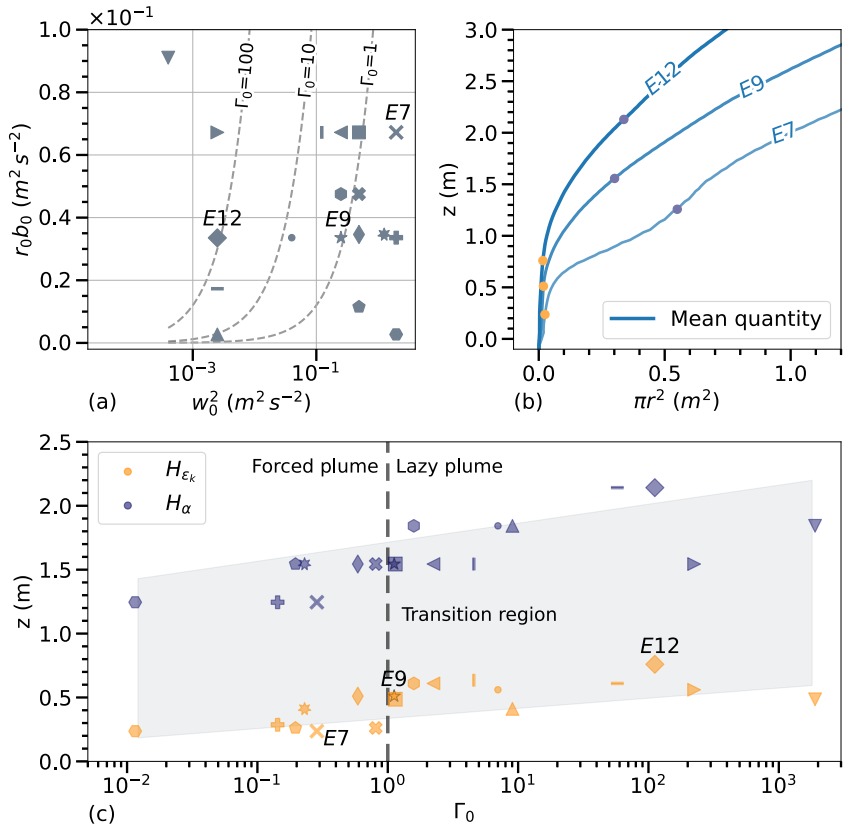

Figure 7. (a) Source conditions for experiments 1 to 18 (see Table 1). (b) The surface of horizontal expansion for three different source conditions, with their transition heights defined by H_{ε_k} (in orange) and H_α (in blue). Notation "E#" denotes the experiment number. (c) Transition heights as a function of Γ_0, the plume source parameter. The dashed line separates the forced and lazy plume regimes, while the gray area encompasses the plume's transitional state.

in Figure 6b represent the profile expected from LES for a thermal sensor placed on the axis. Due to the stirring effect of turbulent structures, the mean profile along the axis is interchangeable with the temperature averaged over a slice bounded by $\sigma = 50$ cm s^{-1}. This indicates that w measurements on the axis are expected to be larger than this σ value.

The in situ profile deviates from the LES profile for two reasons. In practice, the sensor is not perfectly centered, resulting in a colder in situ profile. The in situ profiles correspond better to the mean LES profile for the area bounded by $\sigma = 10$ cm s^{-1}. Second, the thermal inertia of the instrument misses the parcels with the highest fluid temperatures, such as rapidly ascending turbulent structures, as shown by the smaller RMS of the field data than the LES spatial variability.

The consistency of the LES and in situ radius and temperature profiles for $H_{obs} = 60$ cm gives us confidence in the reliability of the LES model in the near-vent region, in contrast to the MTT model. In addition, the good agreement close to the source validates the parameterization of the vent turbulence.

4. Sensitivity to Source Parameters

Hydrothermal plumes can exist under a wide range of conditions, from forced to lazy plume regimes. In this section, we extend the results to a large set of vent source parameters. We provide a detailed description of the transition region from the near-vent to the pure plume regime. The resulting flow field adjustments are analyzed on the basis of plume theory. We use experiments 1 to 18 (Table 1), for which the set of conditions is summarized in Figure 7a, covering most of the parameter space of hydrothermal vents.

4.1. Transition Region

As the plume mixes with the ambient fluid, the potential energy of the density anomaly decreases, and a fraction of it is converted into momentum through the buoyancy flux (Wykes et al., 2015). Therefore, assessing the transition height H_t based on the ratio of forces using the $\Gamma(z)$ parameter becomes complicated because the momentum combines with the kinetic energy resulting from buoyancy. Indeed, several studies have shown that $\Gamma(z)$ exhibits complex behavior before converging to 1 (Hargreaves et al., 2012; Marjanovic et al., 2017; Taub et al., 2015), and its dependence on α further complicates the task.

To address this issue, we frame the transition region using two indicative heights. The first height, H_{ε_k}, corresponds to the location of maximum viscous dissipation, excluding the peak associated with noise injection. A consistent pattern in the vertical profile of viscous dissipation is observed across all results, showing an increase that culminates in a peak within the first meter. This point indicates the establishment of a balance between the shear generated by the injection of momentum and the buoyancy force. The second height, H_α, marks the location where the maximum entrainment of ambient water occurs, indicating the complete destabilization of the plume column into 3D turbulence. As noted by Marjanovic et al. (2017) and Taub et al. (2015), $\alpha(z)$ converges to a constant in the self-similar state. These heights are illustrated in Figure 1b.

Figure 7b shows the rapid horizontal expansion in the transition region for a highly lazy plume (Experiment 12), a plume in balance (Experiment 9), and a forced plume (Experiment 7). H_{ε_k} and H_α effectively capture the transition from vertical streamlines to a turbulent field (Figure 3) and frame the maximum of the derivative $d\log\left(r^2/r_*^2\right)/dz$, where r_* is a reference radius. In Figure 7c, the heights H_{ε_k} and H_α are plotted against the parameter Γ_0. Two key points emerge.

Despite a 6 order of magnitude variation in Γ_0, the transition region exhibits smaller amplitude changes ($\Delta H_{\varepsilon_k} = 0.5$ m and $\Delta H_\alpha = 0.95$ m). This shows that the transition region remains almost invariant to the set of parameters r_0, w_0 and b_0 encountered at the hydrothermal site. H_α ranges from 1.20 to 2.15 m, and H_{ε_k} ranges from 0.25 to 0.75 m, with experiments 7 and 12 differing by a factor of only 1.7. However, a similar trend emerges for both heights H_{ε_k} and H_α. The transition region extends further away from the source as Γ_0 increases. This is consistent with the results of Taub et al. (2015), whose analysis of entrainment rate profiles suggests that lazy plumes reach self-similarity further away from the source than forced plumes.

Forced plumes—up to $\Gamma_0 = 1$—driven by momentum flux are unstable, characterized by intense shear leading to rapid destabilization of the column ($H_{\varepsilon_k} \approx 0.3$ m for $\Gamma_0 < 1$). When the source buoyancy flux balances the input momentum, it slows the development of convective turbulence compared to jet-like plumes ($H_{\varepsilon_k} \approx 0.5$ m for $\Gamma_0 = 1$). In all cases, the flow requires a minimum height of $H_\alpha \approx 1.2$ m to fully develop convective turbulence, even under a highly forced plume regime. It is worth noting that the noise injected at the source accelerates the onset of turbulence.

The second consequence is that the transition region is not sharply delineated, as it extends between H_{ε_k} and H_α. The characteristic length scale, $L_m = M_0^{3/4} B_0^{-1/2}$, has been proposed for forced plumes as the separation between jet-like and plume-like regions by Morton (1959). A similar length scale for lazy plumes, marking the transition to pure plume behavior, is $L_a = Q_0^{3/5} B_0^{-1/5}$ (Hunt & Kaye, 2005). Recent studies by Taub et al. (2015) and Wang and Law (2002) report $z > 5\,L_m$ or $z > 6\,L_m$ as the transition limit between jet-like and plume-like regions. However, these lengths do not accurately represent the hydrothermal plume flow field. For $\Gamma_0 < 1$, $L_m \approx 18$ cm, Figure 7c indicates that the transition to the plume-like region occurs for $z > 8\,L_m$, which is slightly higher but still within reasonable agreement with the literature. In contrast, L_m increases for highly forced plumes, which is not consistent with the trend observed for the LES. For $\Gamma_0 > 1$, $L_a \approx 4$ cm, but convergence to self-similarity clearly occurs at $z > 40\,L_a$.

The high buoyancy flux involved may explain the limited relevance of both L_m and L_a. Our results support the definition of a broader transition region, bounded by H_{ε_k} and H_α, above which the plume reaches a pure plume regime and below which the source conditions dominate. This region is highlighted in gray in Figure 7c, spanning from 0.25 to 2.15 m, and is characteristic of hydrothermal vent conditions. For simplicity, this region is referred to as H_t hereafter. The transition region corresponds to the scale of hydrothermal edifices and falls within the range

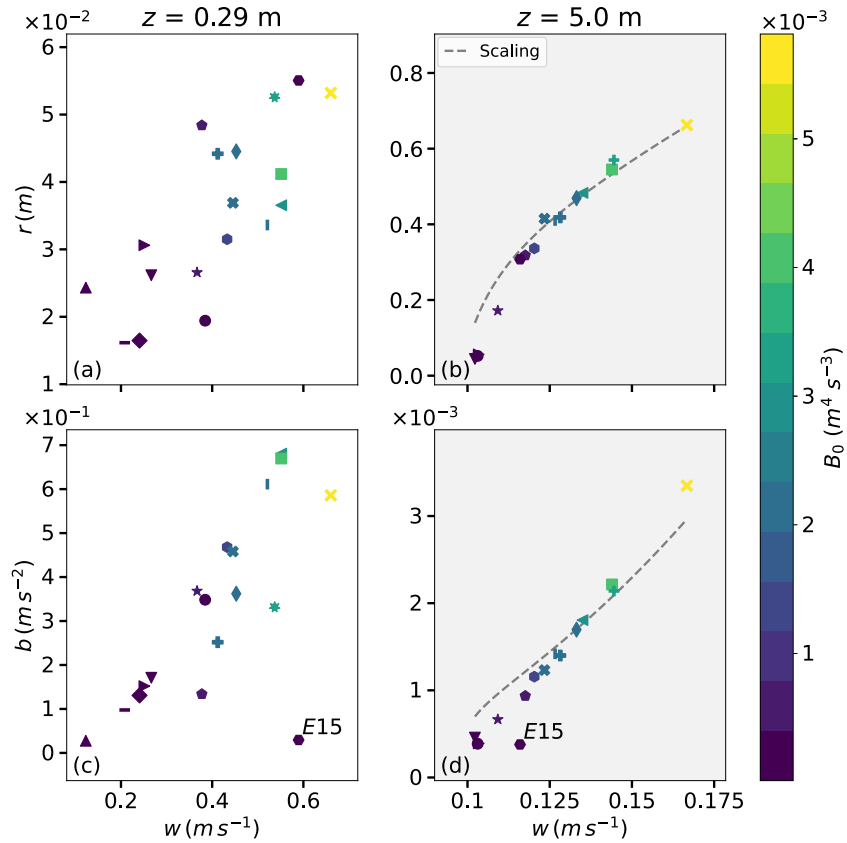

Figure 8. (a and b) Plume radius and (c and d) horizontal mean of buoyancy as a function of vertical velocity for $\sigma = 10$ cm s^{-1} for all experiments in Table 1, except 12, 14, and 16. Each experiment is shown (a and c) below and (b and d) above the transition region identified in Section 4.1. The symbols are colored according to the source buoyancy flux. Notation "E#" denotes the experiment number. Experimental scalings are plotted as dashed lines using Equation 8a in (b) and Equation 8b in (d).

accessible by in situ observational techniques, indicating that hydrothermal plumes observed near the seafloor are typically in a transitional state.

Finally, the minimal effect of b_0 and w_0 on H_t suggests that other factors play a more significant role. H_t is closely related to the vertical extent of the plume, with results showing $H_t \approx H_{nbl}/100$. While variations in r_0 were limited due to small vent sizes and could influence H_t, the parameter N, which was kept constant and is weak enough to assume uniform ambient conditions, has a dominant effect on H_{nbl} due to its larger scaling exponent in Equation 2a. With realistic stratification, H_t remains less than 5% of H_{nbl}, even for the experiment with the lowest B_0 (Experiment 14, where $H_{nbl} = 21$ m from Equation 2a). Thus, it is very likely that achieving a significant change in H_t would require unrealistically high N values to reduce H_{nbl} to a scale comparable to the observed H_t for hydrothermal plumes.

4.2. Organization of the Flow Field

We focus on the relationships between the key flow variables in this transition region. Figure 8 presents the link between r and w, and b and w below ($z = 0.29$ m) and above ($z = 5.0$ m) the transition height, respectively. Each experiment is related to its B_0 value. Consistent relationships indicate that the flow primarily depends on B_0. To limit spatial averaging effects of cold fluid at the plume boundary, we restrict σ to 10 cm s^{-1}. This threshold is too restrictive for experiments with low B_0 and w_0, so experiments 12, 14, and 16 have been excluded from Figures 8b and 8d.

The organization is chaotic in the near-vent region, dominated by vent conditions (Figures 8a and 8c). In contrast, a clear organizational pattern emerges after reaching the pure plume regime (Figures 8b and 8d). The relationships

between r and w, as well as b and w, both collapse to single power-law curves. Wang and Law (2002) showed that the mean axial velocity and turbulent concentration fluctuations similarly collapse into Gaussian curves for both forced and lazy plumes in the pure plume regime.

In Figures 8b and 8d, B_0 governs the overall organization of the flow, setting the levels reached for each key variable above the transition region, where pure plume behavior is observed. The pattern does not depend on the excess force at the source. Consequently, there are no scenarios where one quantity, such as w, becomes disproportionately large while others, such as r or b, remain small. Instead, the system organizes itself to maintain consistency in the overall energy and momentum balance, with all variables adjusting together to reflect the level of B_0 injected.

This is consistent with the buoyancy flux conservation approach in the MTT equations. The derivation of the theoretical model predicts an equilibrium level based solely on B_0 and the ambient stratification (Equations 2a and 2b). The scaling laws obtained from the LES experiments reflect this behavior.

We now examine the scaling laws that explain the alignment of the experimental points in Figures 8b and 8d. To do so, we start from the MTT model in a uniform environment, which is a valid assumption here (see Section 3.1). The right-hand term in Equation 1c vanishes, simplifying the MTT model to the analytical solutions.

$$r \propto z, \tag{6a}$$

$$b \propto B_0^{2/3} z^{-5/3}, \tag{6b}$$

$$w \propto B_0^{1/3} z^{-1/3}. \tag{6c}$$

These equations imply that the buoyancy flux is conserved at all heights. From these scalings, we derive a one-parameter set of new relations that express the relationships between the key plume variables, that is,

$$r \propto B_0^{a} z^{1-a} w^{-3a}, \tag{7a}$$

$$b \propto B_0^{c} z^{-1-c} w^{-3c+2}, \tag{7b}$$

with a and c arbitrary exponents. We used the LES data to optimize these exponents and rounded them to simple rationals. We found $a = 2/3$ and $c = 1/5$. Once the exponents were determined, the nondimensional constant of each scaling was identified through a second optimization, yielding

$$r = 0.262\, B_0^{2/3} z^{1/3} w^{-2}, \tag{8a}$$

$$b = 0.658\, B_0^{1/5} z^{-6/5} w^{7/5}. \tag{8b}$$

Plotting these scalings in Figure 8 requires an additional step: establishing a relationship between B_0 and w. Without this relationship, only $r(w)$ or $b(w)$ could be plotted for a given B_0, which would be irrelevant since the LES cases have different B_0. However, at $z = 5$ m, the LES data exhibit a strong correlation between w and B_0 (not shown), consistent with Equation 6c, though not strictly equal. Therefore, to plot the scalings, we exploited this empirical relationship $B_0(w)$, which we fitted with a cubic polynomial. The third degree is motivated by Equation 6c. This fit is then injected into the derived scalings, Equations 8a and 8b, which are shown in Figures 8b and 8d for r and b, respectively.

As already noted, the agreement with the scaling law improves with height as the distance from the transition region increases, indicating a breakdown of self-similarity in this region. Typically, for plumes with $\Gamma_0 \ll 1$, such as Experiment 15 ($\Gamma_0 = 0.01$), Equation 8b incorrectly predicts high values of b for high values of w. Only when the highly forced plume dissipates its input momentum, it does converge to the solution predicted by the scaling (Figure 8d). However, even at $z = 5$ m, the relationship between b and w has not fully collapsed to the self-similarity solution. Taub et al. (2015) suggests that buoyancy fluctuations are influenced by source conditions over a longer range than velocity fluctuations.

Our results highlight a limitation of the MTT model. Figure 8b shows that r varies with B_0, whereas Equation 6a assumes that r depends only on z. This indicates a difference in the spreading rates, which is consistent with the

experimental results of Kitamura and Sumita (2011). They observe that pure jets have a slightly higher spreading rate than plumes; however, this difference is generally considered to be small (Kotsovinos & List, 1977; Van Reeuwijk et al., 2016).

The overall agreement between the scalings and the LES experiments shows that despite the strong influence of the near-vent region on the flow, the turbulent field can be simplified by scaling laws as plume quantities converge toward self-similarity. This indicates that in the far-field the MTT model captures the underlying physics based on the B_0 value. The LES results highlight that B_0 is the main controlling parameter, even in the exotic hydrothermal regime where high buoyancy flux is injected into weak stratification.

5. Discussion

5.1. Transition Region Observation

The transition region between vent conditions and the pure plume region is identified in an in situ recording of a black smoker at the Tour Eiffel site. The video described below was captured by an ROV and is provided by the authors (Lemaréchal & Matabos, 2023). The comparison is summarized in Figure 9. The source observed here is the same as that used for the in situ measurements in Section 3.5, and Experiment 9 is presented as the numerical counterpart.

We focus first on observations near the seafloor (between 15:10 and 15:44 in the video). The visible plume length is about 60 cm (Figure 9b), while for this source, $H_{\varepsilon_k} = 0.51$ m and $H_\alpha = 1.53$ m. Compared to its numerical equivalent, this limits the analysis to region (1) in Figure 9a, which is dominated by vent conditions. As the ROV ascends (between 16:15 and 18:54), the camera transitions from focusing on the near-vent region through the transition region (gray region labeled 2). At $z \approx 2$ m, the camera reaches the fully buoyant region of the plume (gray region labeled 3—around 17:30), where larger convective structures and fully three-dimensional turbulence dominate (according to LES data, we get $r \approx 0.4$ m, $w \approx 5$ cm s^{-1}). At this height, the mean temperature ($T \approx 7$°C) and the density gradient anomalies associated with the refractive index gradient decrease drastically. The light reflection from plume particles becomes insufficient to distinguish the plume clearly from its surroundings (e.g., at 17:50). In addition, the plume merges with those from neighboring sources, making numerical comparisons or in situ studies of single source plumes extremely challenging.

Region (1) to (2) is the primary source of data for in situ experiments, but this limitation introduces a bias in our understanding of the plume dynamics. By restricting observations to this specific region, we capture a view of the plume that is limited to its near-vent structure, which is strongly influenced by the transition from vent condition to pure plume behavior, where scaling laws fail.

5.2. Impact of Temperature Fluctuations on Tracer Proxies

Temperatures above 40°C have been documented as lethal to various organisms (Bates et al., 2010; Fisher, 1998; Lee et al., 2015). Given the high temperatures typical of black smokers, biotracer survival during transport through the plume might be expected to be unlikely. Consequently, studies often focus on stable environments that exclude such high-temperature conditions, for example, Lee et al. (2015). However, LES results suggest that hydrothermal plumes could serve as a viable vector for biological material transport, as prolonged exposure to high temperatures is unlikely.

Below, we estimate how long particles transported within the first three m of the rising plume are exposed to high and potentially lethal temperatures. To establish a high-temperature threshold of interest, we use the 40°C criterion, which represents a reasonable estimate of the thermal tolerance limit for hydrothermal fauna. We distinguish between the plume's inner core and its outer envelope, numerically defined as the closest cells to the plume boundary. The LES experiment is chosen to reflect the source conditions identified in Section 3.5 (Experiment 9 in Table 1). It provides an actual example of a source in close proximity to a dense faunal community (Van Audenhaege et al., 2022).

Due to computational limitations, an Eulerian approach was chosen over the ideal Lagrangian method. Fixed probes serve as proxies for the trajectory of a particle entrained in the plume. These probes are placed vertically at intervals corresponding to the mesh resolution, either along the plume axis or at its boundary. The envelope probes are positioned at the intersection of the horizontal plane with the contour of the plume volume that satisfies

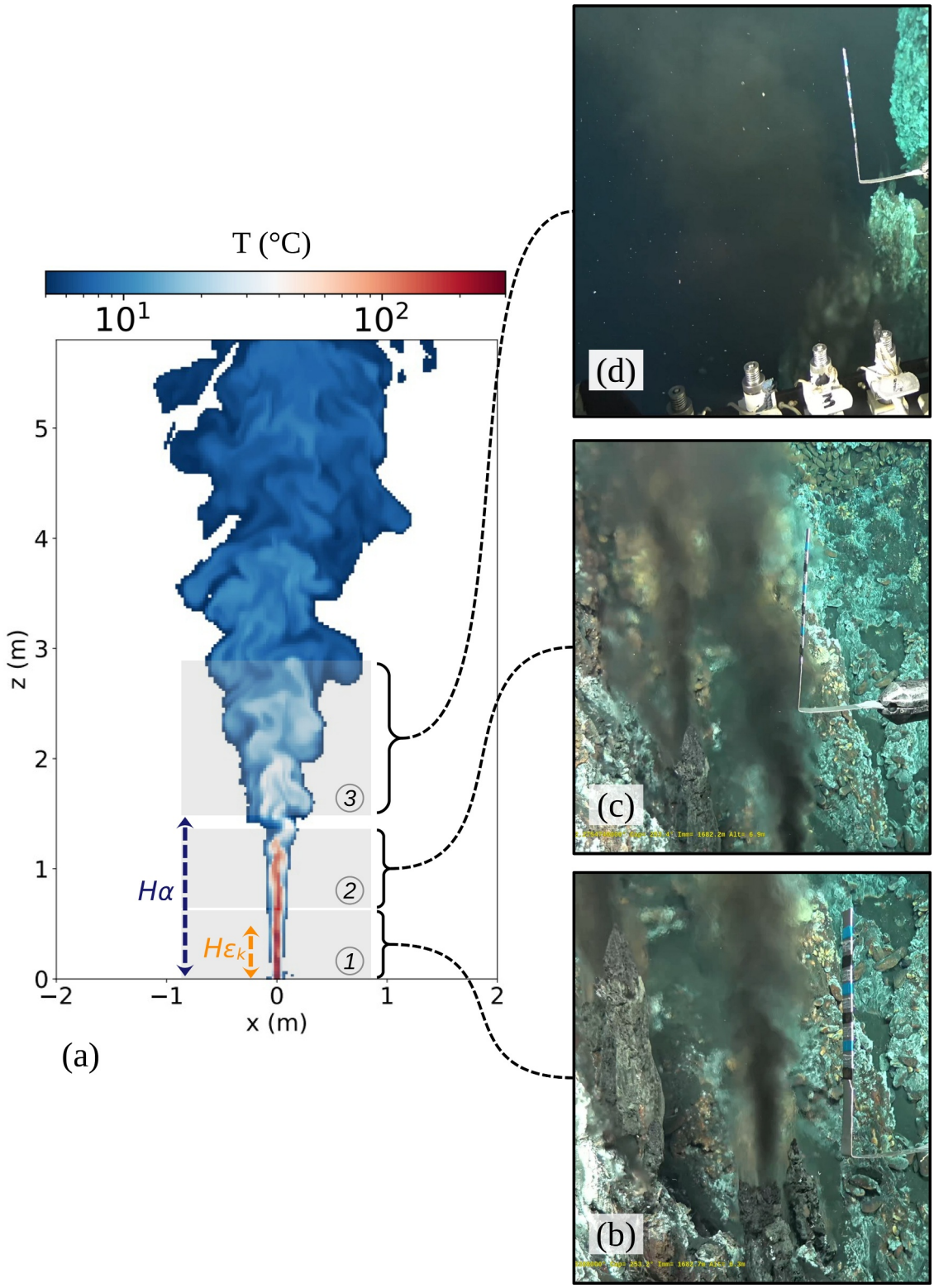

Figure 9. (a) Cross-sectional view of the instantaneous temperature field from a large-eddy simulation experiment (Experiment 9), illustrating three types of regions corresponding to their respective in situ observation windows as viewed during a video-recorded remotely operated vehicle exploration at Tour Eiffel. (b) The view corresponding to the height H_{ε_k}, (c) the view corresponding to H_α, and (d) the region where the plume reached its fully convective turbulent state.

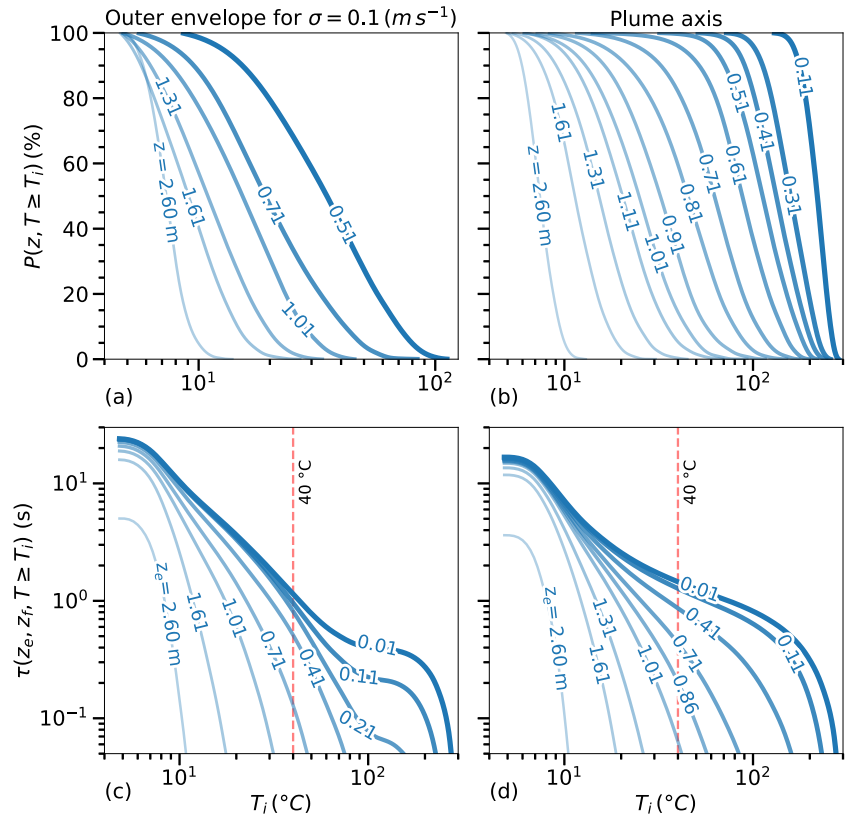

Figure 10. Complementary cumulative distribution function (CCDF) of temperature at different heights z above the vent for Experiment 9, for (a) the plume envelope selected by the criterion $\sigma = 0.1$ m s^{-1} and (b) the plume axis. (c and d) The cumulative time τ spent above each temperature T_i encountered in the hydrothermal fluid for trajectories along the vertical is shown in the same regions. Integration is performed for different starting entry heights z_e inside the plume up to $z_f = 3$ m. (c and d) Plots are truncated below 5×10^{-2} s.

the criterion $\sigma = 0.1$ m s^{-1} on time average. This criterion is consistent with that used to match the in situ data and selects a plume region with sufficient vertical velocity to effectively advect materials. The bias introduced by sampling the plume with a 1D line of probes is mitigated by the large number of measurements taken over time, namely we use a sampling rate of 0.4 s over a duration of 14 min.

Figures 10a and 10b shows the CCDF, $P(z, T \geq T_i)$, derived from the time series of temperature at each fixed probe location. At $z = 80$ cm, the plume axis shows $T > 40$°C events representing 60% of the time distribution, with a maximum temperature of 150°C at this height (Figure 10b). These high temperatures disappear from the core after 1.30 m. Within the envelope, it takes 1 m to eliminate temperatures above 40°C. At 70 cm, such temperatures occur 12% of the time, peaking at 80°C.

The probability distribution alone suggests that a tracer would encounter lethal temperatures in both the core and the envelope of the plume within the first meter above the vent. To investigate this further, we compute the cumulative time τ (s). It is the time taken by a parcel entering the plume at height z_e to reach height z_f, following the trajectory traced by the 1D probe lines, with a temperature exceeding T_i. This computation is performed in the envelope (Figure 10c) and along the plume axis (Figure 10d). The results are integrated from different starting entry heights z_e in the plume up to $z_f = 3$ m, where the temperature has decreased significantly, according to

$$\tau(z_e, z_f, T \geq T_i) = \int_{z_e}^{z_f} \frac{P(z, T \geq T_i)}{w_p(z)} dz, \quad (9)$$

where $w_p(z)$ is the vertical speed at the probe location. The maximum τ for each curve indicates the transit time between z_e and z_f.

The rationale for considering different starting heights z_e is that hydrothermal plumes are often associated with complex local topography, where the fluid comes into contact, providing different entry points for a tracer above the plume source. Below 30 cm, the envelope and core become indistinguishable, resulting in a characteristic bump in the envelope curve, as the cumulative time reflects the core values (Figure 10c), and w_p exceeds the value chosen for σ in this region.

In the envelope, below $z_e = 40$ cm, exposure to temperatures above 40°C lasts for around 1 s, with significant exposure to higher temperatures, for example, more than 0.3 s above 70°C for $z_e = 11$ cm. For a particle entering at 41 cm, exposure to temperatures above 40°C lasts for 0.5 s, with only 5×10^{-2} s above 75°C. Exposure to high temperatures decreases significantly above 70 cm. A trajectory along the axis experiences 0.9 s above 40°C for $z_e = 41$ cm, with a significant duration above very high temperatures compared to the envelope, for example, 0.25 s above 100°C. High temperature exposure along the plume axis becomes negligible only after 1 m. While particle paths are simplified for practical purposes by considering 1D lines, it is important to note that particles could be advected through both regions discussed, and it is essential to assess the viability of tracers as a percentage of success. Nevertheless, both the core and the envelope of the plume show minimal exposure to high temperatures for a particle entrained 1 m above the vent. The envelope is a more favorable region for sustained transport for an entry closer to the vent ($z_e = 40$ cm), considering the temperature levels and the time exposure ratio, than the plume centerline.

These results support the findings of Kim et al. (1994), who demonstrated through dye experiments and the MTT model that a single black smoker can enable substantial vertical transport of larvae, opening pathways to habitats typically inaccessible to near-bottom larvae.

6. Conclusions

Hydrothermal plumes inject a high buoyancy flux into weak stratification, rising from centimeter-scale vents to heights of several hundred meters (Lavelle et al., 2013). They play a key role in vent fields but have been poorly characterized in the near-vent region. To study these plumes, we used an LES approach with AMR to achieve centimeter-scale resolution within a 6-m domain above the vent. Several key points can be highlighted.

First, a typical black smoker (forced plume) is studied to quantify the mean flow and spatial fluctuations, which are difficult to measure in deep-sea vent fields. The mean temperature decreases sharply from $T_0 = 300$°C to $T - T_a = 1.5$°C at $z = 5$ m, and the velocity decreases from $w_0 = 70$ cm s^{-1} to $w = 7$ cm s^{-1}. This results in a substantial volume flow of $Q = 0.25$ m^3 s^{-1} at $z = 5$ m. The plume expands at a nearly constant spreading rate. The results compare well with in situ measurements. While lazy plumes initially accelerate (Marjanovic et al., 2017), we show that forced plumes in the hydrothermal regime also accelerate due to significant buoyancy, reaching $w = 1.14$ m s^{-1}. Numerical approaches to hydrothermal plumes often model a diluted point source above the vent, for example, Adams and Di Iorio (2021); however, approximating a uniform source below $z = 5$ m fails to capture the flow dynamics, especially since turbulence is fully developed at this height.

Secondly, we show that the entrainment rate exhibits strong vertical and temporal variability, associated with the intense mixing required to dissipate the high source buoyancy flux. The overall value in the near-field is $\alpha = 0.19$, which is significantly higher than the classical value of $\alpha = 0.12$ for a pure plume (Richardson & Hunt, 2022; Van Reeuwijk & Craske, 2015). However, the values vary significantly in the vertical, from $\alpha = 0.07$ in the jet-like plume region to $\alpha = 0.15$ in the pure plume region, with much larger values in between. The large variations in $\alpha(z,t)$ are linked to the coherent structures of the turbulent field. Variations reaching up to 90% above the mean profile dilute and homogenize the temperature anomaly distribution, contributing to the flow deceleration. It highlights the main limitation of the MTT model (Morton et al., 1956): α cannot be assumed constant in the near-field. A more appropriate approach would incorporate the work of Wang and Law (2002), who developed a second-order integral model to account for entrainment rate variations, where $\alpha(z)$ is treated as a function of the local Richardson number.

Extreme temperatures ($T > 100$°C) occur for $z < 2$ m, coinciding with the ability of the plume to entrain biotracers from the seafloor. While the limited biological tolerance to high temperatures suggests that particle survival during transport through the plume is unlikely, our study offers a different perspective. For a proxy tracer, exposure times at $T > 40$°C can be as short as 0.5 s in the plume envelope, depending on the height of entrainment, decreasing to 5×10^{-2} s above $T = 75$°C. This challenges the concept of lethal temperatures in dynamic flows. Hydrothermal plumes could thus act as viable vectors for the transport of biological material from the seafloor, supporting the findings of Kim et al. (1994), provided more is known about the ability of the fauna to withstand such conditions for very short periods.

Finally, the sensitivity to source parameters is investigated for the forced and lazy plume regimes. We show that the adjustment from the near-vent region, dominated by source conditions, to the far-field, pure plume regime, leads to the breakdown of self-similar plume behavior in this transition region. This prevents the application of the theoretical model of Morton et al. (1956) in the transition region, which extends from $z = 0.25$ m to $z = 2.15$ m. The transition height shows little sensitivity to the plume regime and would require unrealistic changes in stratification to be significantly affected. Plumes observed at the scale of hydrothermal edifices are typically in a transition state, which may introduce bias into experimental studies at this depth. In the far field, plumes converge to self-similarity and can be described by scalings 8a and 8b derived from plume theory. While the mean quantities do not agree well with the MTT model predictions, the flow field in the pure plume region agrees with the MTT model approach and is primarily organized according to the source buoyancy flux.

Appendix A: Parametric EOS

This section presents the equation of state (EOS) developed for hydrothermal fluids. The EOS is valid in the range of 100–550 bar and 0–350°C at $S_A = 35.2$ g kg^{-1}. A plot of density for different pressure and temperature ranges is shown in Figure A1.

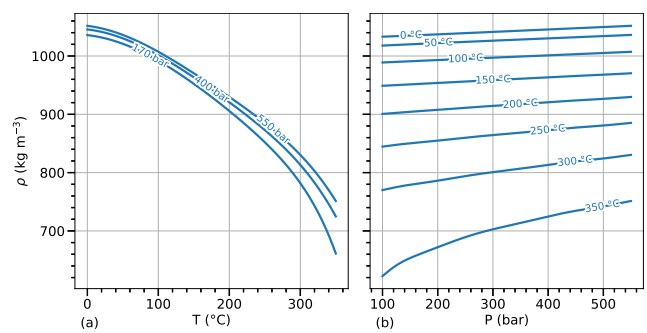

Figure A1. (a) Density of seawater versus temperature calculated by Equation A1 for different levels of pressure. (b) Density versus pressure for different levels of temperature.

The density ρ (kg m^{-3}) as a function of absolute temperature T (°C) and absolute pressure P (bar) is given by

$$\rho(T,P) = A(P)\exp(-B(P)T) + C(P) + D(P)\exp\left(-\frac{(T-E(P))^2}{2F(P)^2}\right), \quad \text{(A1)}$$

where $A(P)$ …$F(P)$ are polynomials in P of the form

$$X(P) = \sum_{i=0}^{8} c_i P^{8-i}, \quad \text{(A2)}$$

with c_i being the polynomial coefficients given in Table A1 for each parameter. A code sample to compute this equation is provided by the authors (Lemaréchal et al., 2024b). To spare computing resources during calculations, we recommend generating an EOS table with a fixed step for efficient data interpolation through array indexing.

Journal of Geophysical Research: Oceans

10.1029/2024JC022277

Table A1
Polynomial Coefficients of Equation A2

	0	1	2	3	4	5	6	7	8
A	−7.01307390e−21	1.95660070e−17	−2.23352820e−14	1.30848310e−11	−3.97395990e−09	5.53535930e−07	−3.96405330e−05	1.37810860e−03	−1.62833820e−02
B	−2.04801770e−22	5.85654850e−19	−7.17814260e−16	4.93110400e−13	−2.08500570e−10	5.61590670e−08	−9.67436850e−06	1.04954760e−03	−7.55052580e−02
C	−9.08091870e−18	2.56711040e−14	−3.09991740e−11	2.08730680e−08	−8.57874330e−06	2.21278690e−03	−3.54404280e−01	3.36599270e+01	−7.59305030e+02
D	9.14772610e−18	−2.58613080e−14	3.12300980e−11	−2.10288630e−08	8.64259430e−06	−2.22918380e−03	3.57047310e−01	−3.38666710e+01	1.79999190e+03
E	−2.57551460e−19	7.36404340e−16	−9.02945380e−13	6.20751900e−10	−2.62358970e−07	7.01422040e−05	−1.17048000e−02	1.14665420e+00	−7.20442180e+01
F	2.80580730e−18	−7.95146740e−15	9.63263680e−12	−6.51411210e−09	2.69367930e−06	−7.01266430e−04	1.14048660e−01	−1.11301910e+01	7.25953200e+02

Conflict of Interest

The authors declare no conflicts of interest relevant to this study.

Data Availability Statement

The simulations were performed using the open-source Basilisk code, obtained from the official repository in Popinet (2013), release 21-05-05. Model code, including input files and an example output for Experiment 1 are available at Lemaréchal et al. (2025). The real-time sequence of the turbulent field observed with the λ_2 technique is described in Lemaréchal et al. (2024a). The in situ recording of a black smoker is available in 4K resolution (Lemaréchal & Matabos, 2023) and accessible in 720p resolution at https://video.ifremer.fr/video?id=52548. A code to compute the parametric EOS is described in Lemaréchal et al. (2024b).

Acknowledgments
The authors acknowledge support from Université de Bretagne Occidentale, the iAtlantic project (Grant 818123) supported by the European Union's Horizon 2020 (H2020) program, the LOPS, and the Interdisciplinary Graduate School for the Blue Planet project (ANR-17-EURE-0015). This work was performed using HPC resources from GENCI-TGCC (Grant 2022-A0090112051). We warmly thank the crews of L'Atalante who participated in the MoMARSAT cruises. We also acknowledge M. Matabos, P.-M. Sarradin, and M. Cannat for coleading and managing the MoMARSAT cruises and the EMSO-Azores observatory. We thank the editor and the anonymous reviewers for their thoughtful comments and suggestions, which helped improve the quality of this work.

References

Adams, I., & Di Iorio, D. (2021). Turbulence properties of a deep-sea hydrothermal plume in a time-variable cross-flow: Field and model comparisons for dante in the main endeavour field. *Journal of Geophysical Research: Oceans*, *126*(9), e2020JC016638. https://doi.org/10.1029/2020JC016638

Barreyre, T., Escartín, J., Garcia, R., Cannat, M., Mittelstaedt, E., & Prados, R. (2012). Structure, temporal evolution, and heat flux estimates from the lucky strike deep-sea hydrothermal field derived from seafloor image mosaics. *Geochemistry, Geophysics, Geosystems*, *13*(4). https://doi.org/10.1029/2011GC003990

Barreyre, T., Escartín, J., Sohn, R. A., Cannat, M., Ballu, V., & Crawford, W. C. (2014). Temporal variability and tidal modulation of hydrothermal exit-fluid temperatures at the lucky strike deep-sea vent field, mid-atlantic ridge. *Journal of Geophysical Research: Solid Earth*, *119*(4), 2543–2566. https://doi.org/10.1002/2013JB010478

Bates, A. E., Lee, R. W., Tunnicliffe, V., & Lamare, M. D. (2010). Deep-sea hydrothermal vent animals seek cool fluids in a highly variable thermal environment. *Nature Communications*, *1*(1), 14. https://doi.org/10.1038/ncomms1014

Bell, J. B., Colella, P., & Glaz, H. M. (1989). A second-order projection method for the incompressible navier-stokes equations. *Journal of Computational Physics*, *85*(2), 257–283. https://doi.org/10.1016/0021-9991(89)90151-4

Bemis, K. G., Silver, D., Xu, G., Light, R., Jackson, D., Jones, C., et al. (2015). The path to covis: A review of acoustic imaging of hydrothermal flow regimes. *Deep Sea Research Part II: Topical Studies in Oceanography*, *121*, 159–176. https://doi.org/10.1016/j.dsr2.2015.06.002

Bischoff, J. L., & Rosenbauer, R. J. (1985). An empirical equation of state for hydrothermal seawater (3.2 percent nacl). *American Journal of Science*, *285*(8), 725–763. https://doi.org/10.2475/ajs.285.8.725

Chavagnac, V., Ali, H. S., Jeandel, C., Leleu, T., Destrigneville, C., Castillo, A., et al. (2018). Sulfate minerals control dissolved rare Earth element flux and nd isotope signature of buoyant hydrothermal plume (emso-azores, 37 n mid-atlantic ridge). *Chemical Geology*, *499*, 111–125. https://doi.org/10.1016/j.chemgeo.2018.09.021

Ciriello, F., & Hunt, G. (2020). Analytical solutions and virtual origin corrections for forced, pure and lazy turbulent plumes based on a universal entrainment function. *Journal of Fluid Mechanics*, *893*, A12. https://doi.org/10.1017/jfm.2020.225

Cotte, L., Chavagnac, V., Pelleter, E., Laës-Huon, A., Cathalot, C., Dulaquais, G., et al. (2020). Metal partitioning after in situ filtration at deep-sea vents of the lucky strike hydrothermal field (emso-azores, mid-atlantic ridge, 37 n). *Deep Sea Research Part I: Oceanographic Research Papers*, *157*, 103204. https://doi.org/10.1016/j.dsr.2019.103204

Crone, T. J., McDuff, R. E., & Wilcock, W. S. (2008). Optical plume velocimetry: A new flow measurement technique for use in seafloor hydrothermal systems. *Experiments in Fluids*, *45*(5), 899–915. https://doi.org/10.1007/s00348-008-0508-2

Daskiran, C., Cui, F., Boufadel, M. C., Zhao, L., Socolofsky, S. A., Ozgokmen, T., et al. (2020). Hydrodynamics and dilution of an oil jet in crossflow: The role of small-scale motions from laboratory experiment and large eddy simulations. *International Journal of Heat and Fluid Flow*, *85*, 108634. https://doi.org/10.1016/j.ijheatfluidflow.2020.108634

Davies, J. H., & Davies, D. R. (2010). Earth's surface heat flux. *Solid Earth*, *1*(1), 5–24. https://doi.org/10.5194/se-1-5-2010

Devenish, B., Rooney, G., & Thomson, D. (2010). Large-eddy simulation of a buoyant plume in uniform and stably stratified environments. *Journal of Fluid Mechanics*, *652*, 75–103. https://doi.org/10.1017/S0022112010000017

Fabregat, A., Dewar, W. K., Özgökmen, T. M., Poje, A. C., & Wienders, N. (2015). Numerical simulations of turbulent thermal, bubble and hybrid plumes. *Ocean Modelling*, *90*, 16–28. https://doi.org/10.1016/j.ocemod.2015.03.007

Fabregat, A., Poje, A. C., Özgökmen, T. M., & Dewar, W. K. (2016a). Dynamics of multiphase turbulent plumes with hybrid buoyancy sources in stratified environments. *Physics of Fluids*, *28*(9), 095109. https://doi.org/10.1063/1.4963313

Fabregat, A., Poje, A. C., Özgökmen, T. M., & Dewar, W. K. (2016b). Effects of rotation on turbulent buoyant plumes in stratified environments. *Journal of Geophysical Research: Oceans*, *121*(8), 5397–5417. https://doi.org/10.1002/2016JC011737

Fiedler, H. (1988). Coherent structures in turbulent flows. *Progress in Aerospace Sciences*, *25*(3), 231–269. https://doi.org/10.1016/0376-0421(88)90001-2

Fisher, C. R. (1998). Temperature and sulphide tolerance of hydrothermal vent fauna. *Cahiers de Biologie Marine*, *39*(3–4), 283–286.

Fontaine, F. J., Cannat, M., Escartin, J., & Crawford, W. C. (2014). Along-axis hydrothermal flow at the axis of slow spreading mid-ocean ridges: Insights from numerical models of the lucky strike vent field (mar). *Geochemistry, Geophysics, Geosystems*, *15*(7), 2918–2931. https://doi.org/10.1002/2014GC005372

Fox, D. G. (1970). Forced plume in a stratified fluid. *Journal of Geophysical Research*, *75*(33), 6818–6835. https://doi.org/10.1029/JC075i033p06818

Gao, X., Dong, C., Liang, J., Yang, J., Li, G., Wang, D., & McWilliams, J. C. (2019). Convective instability-induced mixing and its parameterization using large eddy simulation. *Ocean Modelling*, *137*, 40–51. https://doi.org/10.1016/j.ocemod.2019.03.008

Girard, F., Sarrazin, J., Arnaubec, A., Cannat, M., Sarradin, P.-M., Wheeler, B., & Matabos, M. (2020). Currents and topography drive assemblage distribution on an active hydrothermal edifice. *Progress in Oceanography*, *187*, 102397. https://doi.org/10.1016/j.pocean.2020.102397

Hargreaves, D. M., Scase, M. M., & Evans, I. (2012). A simplified computational analysis of turbulent plumes and jets. *Environmental Fluid Mechanics*, *12*(6), 555–578. https://doi.org/10.1007/s10652-012-9250-7

Hunt, G., & Kaye, N. (2001). Virtual origin correction for lazy turbulent plumes. *Journal of Fluid Mechanics*, *435*, 377–396. https://doi.org/10.1017/S0022112001003871

Hunt, G., & Kaye, N. (2005). Lazy plumes. *Journal of Fluid Mechanics*, *533*, 329–338. https://doi.org/10.1017/S002211200500457X

IOC, SCOR, IAPSO, et al. (2010). The international thermodynamic equation of seawater, 2010: Calculation and use of thermodynamic properties.

Jeong, J., & Hussain, F. (1995). On the identification of a vortex. *Journal of Fluid Mechanics*, *285*, 69–94. https://doi.org/10.1017/S0022112095000462

Jiang, H., & Breier, J. A. (2014). Physical controls on mixing and transport within rising submarine hydrothermal plumes: A numerical simulation study. *Deep Sea Research Part I: Oceanographic Research Papers*, *92*, 41–55. https://doi.org/10.1016/j.dsr.2014.06.006

Kaye, N. (2008). Turbulent plumes in stratified environments: A review of recent work. *Atmosphere-Ocean*, *46*(4), 433–441. https://doi.org/10.3137/ao.460404

Kim, S. L., Mullineaux, L. S., & Helfrich, K. R. (1994). Larval dispersal via entrainment into hydrothermal vent plumes. *Journal of Geophysical Research*, *99*(C6), 12655–12665. https://doi.org/10.1029/94JC00644

Kitamura, S., & Sumita, I. (2011). Experiments on a turbulent plume: Shape analyses. *Journal of Geophysical Research*, *116*(B3), B03208. https://doi.org/10.1029/2010JB007633

Koschinsky, A., Garbe-Schönberg, D., Sander, S., Schmidt, K., Gennerich, H.-H., & Strauss, H. (2008). Hydrothermal venting at pressure-temperature conditions above the critical point of seawater, 5 s on the mid-atlantic ridge. *Geology*, *36*(8), 615–618. https://doi.org/10.1130/G24726A.1

Kotsovinos, N. E., & List, E. J. (1977). Plane turbulent buoyant jets. Part 1. Integral properties. *Journal of Fluid Mechanics*, *81*(1), 25–44. https://doi.org/10.1017/S002211207700189X

Lavelle, J., Di Iorio, D., & Rona, P. (2013). A turbulent convection model with an observational context for a deep-sea hydrothermal plume in a time-variable cross flow. *Journal of Geophysical Research: Oceans*, *118*(11), 6145–6160. https://doi.org/10.1002/2013JC009165

Lee, R. W., Robert, K., Matabos, M., Bates, A. E., & Juniper, S. K. (2015). Temporal and spatial variation in temperature experienced by macrofauna at main endeavour hydrothermal vent field. *Deep Sea Research Part I: Oceanographic Research Papers*, *106*, 154–166. https://doi.org/10.1016/j.dsr.2015.10.004

Lemaréchal, C., & Matabos, M. (2023). *Recording of a black smoker at the tour eiffel vent field during momarsat2023*. SEANOE. https://doi.org/10.17882/103869

Lemaréchal, C., Roullet, G., & Gula, J. (2024a). Coherent structures of a hydrothermal buoyant plume in the near-field obtained through les at ultra-high resolution. *Zenodo*. https://doi.org/10.5281/zenodo.13829868

Lemaréchal, C., Roullet, G., & Gula, J. (2024b). Parametric equation of state of seawater for hydrothermal vent conditions. *Zenodo*. https://doi.org/10.5281/zenodo.14332032

Lemaréchal, C., Roullet, G., & Gula, J. (2025). Basilisk simulation setup and model output for hydrothermal plume near-field dynamics from les and observations. *Zenodo*. https://doi.org/10.5281/zenodo.17109121

Marjanovic, G., Taub, G., & Balachandar, S. (2017). On the evolution of the plume function and entrainment in the near-source region of lazy plumes. *Journal of Fluid Mechanics*, *830*, 736–759. https://doi.org/10.1017/jfm.2017.622

Matulka, A., López, P., Redondo, J., & Tarquis, A. (2014). On the entrainment coefficient in a forced plume: Quantitative effects of source parameters. *Nonlinear Processes in Geophysics*, *21*(1), 269–278. https://doi.org/10.5194/npg-21-269-2014

McDougall, T. J., Jackett, D. R., Wright, D. G., & Feistel, R. (2003). Accurate and computationally efficient algorithms for potential temperature and density of seawater. *Journal of Atmospheric and Oceanic Technology*, *20*(5), 730–741. https://doi.org/10.1175/1520-0426(2003)20<730:aaceaf>2.0.co;2

Mittelstaedt, E., Escartín, J., Gracias, N., Olive, J.-A., Barreyre, T., Davaille, A., et al. (2012). Quantifying diffuse and discrete venting at the tour eiffel vent site, lucky strike hydrothermal field. *Geochemistry, Geophysics, Geosystems*, *13*(4). https://doi.org/10.1029/2011GC003991

Morton, B. (1959). Forced plumes. *Journal of Fluid Mechanics*, *5*(1), 151–163. https://doi.org/10.1017/S002211205900012X

Morton, B., & Middleton, J. (1973). Scale diagrams for forced plumes. *Journal of Fluid Mechanics*, *58*(1), 165–176. https://doi.org/10.1017/S002211207300220X

Morton, B., Taylor, G. I., & Turner, J. S. (1956). Turbulent gravitational convection from maintained and instantaneous sources. *Proceedings of the Royal Society of London. Series A. Mathematical and Physical Sciences*, *234*(1196), 1–23. https://doi.org/10.1098/rspa.1956.0011

Mullineaux, L. S., & France, S. C. (1995). Dispersal mechanisms of deep-sea hydrothermal vent fauna. *Geophysical Monograph Series*, *91*, 408–424. https://doi.org/10.1029/GM091p0408

Pham, M., Plourde, F. d. r., & Kim, S. D. (2005). Three-dimensional characterization of a pure thermal plume. *Journal of Heat Transfer*, *127*(6), 624–636. https://doi.org/10.1115/1.1863275

Plourde, F., Pham, M. V., Kim, S. D., & Balachandar, S. (2008). Direct numerical simulations of a rapidly expanding thermal plume: Structure and entrainment interaction. *Journal of Fluid Mechanics*, *604*, 99–123. https://doi.org/10.1017/S0022112008001006

Popinet, S. (2003). Gerris: A tree-based adaptive solver for the incompressible euler equations in complex geometries. *Journal of Computational Physics*, *190*(2), 572–600. https://doi.org/10.1016/S0021-9991(03)00298-5

Popinet, S. (2009). An accurate adaptive solver for surface-tension-driven interfacial flows. *Journal of Computational Physics*, *228*(16), 5838–5866. https://doi.org/10.1016/j.jcp.2009.04.042

Popinet, S. (2013). The basilisk code, release 21-05-05. Retrieved from http://basilisk.fr/

Popinet, S. (2015). A quadtree-adaptive multigrid solver for the Serre–green–Naghdi equations. *Journal of Computational Physics*, *302*, 336–358. https://doi.org/10.1016/j.jcp.2015.09.009

Priestley, C., & Ball, F. (1955). Continuous convection from an isolated source of heat. *Quarterly Journal of the Royal Meteorological Society*, *81*(348), 144–157. https://doi.org/10.1002/qj.49708134803

Richardson, J., & Hunt, G. R. (2022). What is the entrainment coefficient of a pure turbulent line plume? *Journal of Fluid Mechanics*, *934*, A11. https://doi.org/10.1017/jfm.2021.1070

Safarov, J., Millero, F., Feistel, R., Heintz, A., & Hassel, E. (2009). Thermodynamic properties of standard seawater: Extensions to high temperatures and pressures. *Ocean Science*, *5*(3), 235–246. https://doi.org/10.5194/os-5-235-2009

Sarrazin, J., Rodier, P., Tivey, M. K., Singh, H., Schultz, A., & Sarradin, P.-M. (2009). A dual sensor device to estimate fluid flow velocity at diffuse hydrothermal vents. *Deep Sea Research Part I: Oceanographic Research Papers*, *56*(11), 2065–2074. https://doi.org/10.1016/j.dsr.2009.06.008

Sclater, J., Jaupart, C., & Galson, D. (1980). The heat flow through oceanic and continental crust and the heat loss of the earth. *Reviews of Geophysics*, *18*(1), 269–311. https://doi.org/10.1029/RG018i001p00269

Shabbir, A., & George, W. K. (1994). Experiments on a round turbulent buoyant plume. *Journal of Fluid Mechanics*, *275*, 1–32. https://doi.org/10.1017/S0022112094002260

Speer, K. G., & Rona, P. A. (1989). A model of an atlantic and pacific hydrothermal plume. *Journal of Geophysical Research*, *94*(C5), 6213–6220. https://doi.org/10.1029/JC094iC05p06213

Sun, H., Feistel, R., Koch, M., & Markoe, A. (2008). New equations for density, entropy, heat capacity, and potential temperature of a saline thermal fluid. *Deep Sea Research Part I: Oceanographic Research Papers*, *55*(10), 1304–1310. https://doi.org/10.1016/j.dsr.2008.05.011

Tao, Y., Rosswog, S., & Brüggen, M. (2013). A simulation modeling approach to hydrothermal plumes and its comparison to analytical models. *Ocean Modelling*, *61*, 68–80. https://doi.org/10.1016/j.ocemod.2012.10.001

Taub, G., Lee, H., Balachandar, S., & Sherif, S. (2015). An examination of the high-order statistics of developing jets, lazy and forced plumes at various axial distances from their source. *Journal of Turbulence*, *16*(10), 950–978. https://doi.org/10.1080/14685248.2015.1008006

Thurnherr, A., & Richards, K. (2001). Hydrography and high-temperature heat flux of the rainbow hydrothermal site (36 14' n, mid-atlantic ridge). *Journal of Geophysical Research*, *106*(C5), 9411–9426. https://doi.org/10.1029/2000JC900164

Van Audenhaege, L., Matabos, M., Brind'Amour, A., Drugmand, J., Laës-Huon, A., Sarradin, P.-M., & Sarrazin, J. (2022). Long-term monitoring reveals unprecedented stability of a vent mussel assemblage on the mid-atlantic ridge. *Progress in Oceanography*, *204*, 102791. https://doi.org/10.1016/j.pocean.2022.102791

Van Dover, C. L. (2002). Community structure of mussel beds at deep-sea hydrothermal vents. *Marine Ecology Progress Series*, *230*, 137–158. https://doi.org/10.3354/meps230137

Van Reeuwijk, M., & Craske, J. (2015). Energy-consistent entrainment relations for jets and plumes. *Journal of Fluid Mechanics*, *782*, 333–355. https://doi.org/10.1017/jfm.2015.534

Van Reeuwijk, M., Salizzoni, P., Hunt, G. R., & Craske, J. (2016). Turbulent transport and entrainment in jets and plumes: A dns study. *Physical Review Fluids*, *1*(7), 074301. https://doi.org/10.1103/PhysRevFluids.1.074301

Vic, C., Gula, J., Roullet, G., & Pradillon, F. (2018). Dispersion of deep-sea hydrothermal vent effluents and larvae by submesoscale and tidal currents. *Deep Sea Research Part I: Oceanographic Research Papers*, *133*, 1–18. https://doi.org/10.1016/j.dsr.2018.01.001

Vreman, A. (2004). An eddy-viscosity subgrid-scale model for turbulent shear flow: Algebraic theory and applications. *Physics of Fluids*, *16*(10), 3670–3681. https://doi.org/10.1063/1.1785131

Wang, H., & Law, A. W.-k. (2002). Second-order integral model for a round turbulent buoyant jet. *Journal of Fluid Mechanics*, *459*, 397–428. https://doi.org/10.1017/S0022112002008157

Winters, K. B., Lombard, P. N., Riley, J. J., & D'Asaro, E. A. (1995). Available potential energy and mixing in density-stratified fluids. *Journal of Fluid Mechanics*, *289*, 115–128. https://doi.org/10.1017/S002211209500125X

Woods, A. W. (2010). Turbulent plumes in nature. *Annual Review of Fluid Mechanics*, *42*(1), 391–412. https://doi.org/10.1146/annurev-fluid-121108-145430

Wykes, M. S. D., Hughes, G. O., & Dalziel, S. B. (2015). On the meaning of mixing efficiency for buoyancy-driven mixing in stratified turbulent flows. *Journal of Fluid Mechanics*, *781*, 261–275. https://doi.org/10.1017/jfm.2015.462

Xu, G., Jackson, D., Bemis, K., & Rona, P. (2013). Observations of the volume flux of a seafloor hydrothermal plume using an acoustic imaging sonar. *Geochemistry, Geophysics, Geosystems*, *14*(7), 2369–2382. https://doi.org/10.1002/ggge.20177

Xu, G., McGillicuddy Jr, D., Mills, S., & Mullineaux, L. (2018). Dispersal of hydrothermal vent larvae at east pacific rise 9–10 n segment. *Journal of Geophysical Research: Oceans*, *123*(11), 7877–7895. https://doi.org/10.1029/2018JC014290